Seismic and aseismic fault growth lead to different fault orientations

Simon Preuss[1], Robert Herrendörfer[1,2,4], Taras Gerya[1], Jean Paul Ampuero[3], Ylona van Dinther[2,5]

[1]Geophysical Fluid Dynamics, Institute of Geophysics, Department of Earth sciences, ETH Zürich, 8092 Zürich, Switzerland

[2]Seismology and Wave Physics, Institute of Geophysics, Department of Earth sciences, ETH Zürich, 8092 Zürich, Switzerland

[3]Géoazur Laboratory, Institut de Recherche pour le Développement - Université Côte d'Azur, Campus Azur du CNRS, 06560 Valbonne, France

[4]Institute of Computational Physics, School of Engineering, ZHAW Zurich University of Applied Sciences, 8400 Winterthur, Switzerland

[5]Tectonics, Department of Earth Sciences, Utrecht University, Princetonlaan 4, 3584 CB, Utrecht, the Netherlands

Key Points:

- Numerical model combining visco-elasto-plasticity, rate-and-state friction and elastodynamics simulates the growth of strike-slip faults
- Two distinct fault growth modes, seismic and aseismic, can be distinguished by their fault orientation relative to regional stresses
- The model explains altered stress orientations during the genesis of the Landers-Mojave fault system

---

Corresponding author: Simon Preuss, `sipreuss@ethz.ch`

Abstract

Orientations of natural fault systems are subject to large variations. They often contradict classical Andersonian faulting theory as they are misoriented relative to the prevailing regional stress field. This is ascribed to local effects of structural or stress heterogeneities and reorientations of structures or stresses on the long-term. To better understand the relation between fault orientation and regional stresses, we simulate spontaneous fault growth and its effect on the stress field. Our approach incorporates earthquake rupture dynamics, visco-elasto-plastic brittle deformation and a rate-and state-dependent friction formulation in a continuum mechanics framework. We investigate how strike slip faults orient according to local and far-field stresses during their growth. We identify two modes of fault growth, seismic and aseismic, distinguished by different fault angles and slip velocities. Seismic fault growth causes a significant elevation of dynamic stresses and friction values ahead of the propagating fault tip. These elevated quantities result in a greater strike angle relative to the maximum principal regional stress than that of a fault segment formed aseismically. When compared to the near-tip time-dependent stress field the fault orientations produced by both growth modes follow Anderson's classical faulting theory. We demonstrate how the two types of fault growth may be distinguished in natural faults by comparing their angles relative to the original regional maximum principal stress. A stress field analysis of the Landers-Mojave fault suggests that an angle greater than approximately 25° between two faults indicates seismic fault growth.

1 Introduction

Hundreds of kilometers long strike slip faults formed from smaller defects (e.g. Hirsch, 1975; Regenauer-Lieb et al., 2006; Regenauer-Lieb & Yuen, 2003) and grow larger as they accommodate more strain (e.g. Nur, Ron, & Beroza, 1993; Perrin, Manighetti, Ampuero, Cappa, & Gaudemer, 2016; Perrin, Manighetti, & Gaudemer, 2016). The classical understanding of fault growth relates fault length linearly to accumulated displacement due to episodically recurring earthquakes (e.g. Bürgmann, Pollard, & Martel, 1994; Cowie & Scholz, 1992a, 1992b; Manighetti, King, & Sammis, 2004; Manighetti, King, & Gaudemer, 2001; Norris & Toy, 2014; Peacock, 1991; Peacock & Sanderson, 1996; Perrin, Manighetti, Ampuero, et al., 2016; Perrin, Manighetti, & Gaudemer, 2016; Scholz & Lawler, 2004; Segall & Pollard, 1983). A larger fault length, and therefore a larger fault area, augments the potential to generate bigger earthquakes and changes the frequency-magnitude statistics (e.g. Ben-Zion, 2008; Dal Zilio, van Dinther, Gerya, & Pranger, 2018; Ross, Hauksson, & Ben-Zion, 2017). Faults are two-dimensional surfaces that can expand at different angles with respect to horizontal and vertical planes. A strike slip fault is, however, typically a vertical or sub-vertical dipping plane (e.g. Kim, Hong, Lee, & Taira, 2016; R. Sibson, Ghisetti, & Ristau, 2011; Simpson, 1997; Woodcock & Fischer, 1986; M. D. Zoback et al., 1987) as described first by Anderson (1905) in his 'Andersonian faulting theory'. Vertical fault growth is limited by the brittle-ductile transition. Therefore, the fault strike angle is an important degree of freedom of a laterally expanding strike-slip fault. Laboratory experiments, numerical simulations and theoretical studies investigated the angle α between a new forming, mechanically stable fault and the maximum principal compressional stress direction σ_1 (e.g. Arthur, Dunstan, Al-Ani, & Assadi, 1977; Choi & Petersen, 2015; Kaus, 2010; Vermeer, 1990; Zang & Stephansson, 2010, p. 39). They demonstrated that the angle α follows one of the three types:

Roscoe angle:

$$\alpha_{R_{1-4}} = \pm\left(\frac{\pi}{4} \mp \frac{\psi}{2}\right), \tag{1}$$

Coulomb angle:

$$\alpha_{C_{1-4}} = \pm\left(\frac{\pi}{4} \mp \frac{\varphi}{2}\right), \tag{2}$$

Arthur angle:

$$\alpha_{A_{1-4}} = \pm\left(\frac{\pi}{4} \mp \frac{\varphi+\psi}{4}\right), \tag{3}$$

where ψ is the dilation angle that represents volumetric change in shear deformations and φ is the internal angle of friction, related to μ, the friction coefficient, as $\mu = \tan\varphi$. The Roscoe and Coulomb angles are upper and lower bounds, and the Arthur angle is defined as the mean of these two angles (Arthur et al., 1977). In general, the Arthur angle is a good approximation of the fault angle α (Choi & Petersen, 2015). Equations 1-3 yield four potential fracture surface orientations for each of the three individual fault angle types. All four angles are equally valid, the reason for favoring one over the other three is explained in section 2.1.

When compared to natural observations, the angle at which new faults form is controversial. Fault angles in nature are often substantially distinct from the ones predicted by the Mohr-Coulomb failure criterion (appendix A) and Andersonian faulting theory (e.g. Fletcher, Oskin, & Teran, 2016; Hardebeck & Michael, 2004; Scholz, Ando, & Shaw, 2010; R. Sibson et al., 2011; R. H. Sibson, 1990; Townend & Zoback, 2004). This is already shown in Anderson's first publication (Anderson, 1905). Faults form according to the state of stress prevailing at the time of genesis of the structure. Since the orientation of the stress field adapts to changing tectonic conditions, the structure is very likely not correlated with the current stress field (Zang & Stephansson, 2010, p. 247). A boundary element modeling study showed that the propagation path of an isolated fault depends on both far-field stresses and fault friction (Du & Aydin, 1995). This might be true for quasi-static fault growth, during which near-fault and far-field stresses are not changing substantially and are oriented similarly. However, dynamic effects strongly distort elastically predicted stress fields near rapidly propagating crack tips. This is due to an increase of the maximum off-fault shear stress relative to that on the main fault with the velocity V_r of rupture propagation (Poliakov, Dmowska, & Rice, 2002).

Following both lines of argument we formulate our first hypothesis: When assessing fault angles, local instantaneous near-tip stress field and friction coefficient need to be taken into account during all phases of fault formation, rather than usually available far-field or post-formation quantities. We suppose that during quasi-static fault growth far-field and local stress orientations deviate insignificantly, while only far-field stress orientations are insignificantly altered during dynamic fault growth.

This last assumption leads to our second hypothesis. Fracture mechanics predicts that both aseismic and seismic fault slip produce stress concentrations at a fault's edges. These elevated stresses generate damage at the fault ends, which promotes fault growth. Indeed, part of the damage related to fault growth occurs dynamically during earthquakes (e.g. Andrews, 2005; Manighetti, Campillo, Sammis, Mai, & King, 2005; Perrin, Manighetti, Ampuero, et al., 2016; Schaff & Beroza, 2004). The other part of crustal damage might be driven by static stress concentration near growing fault tips (e.g. Aydin & Berryman, 2010; Cooke, 1997; Lehner, Li, & Rice, 1981; Perrin, Manighetti, Ampuero, et al., 2016; Willemse & Pollard, 1998). The result are slowly moving disturbances of aseismic deformation (Ida, 1974) indicating that fault creep is kinematically similar to seismic faulting and may be sizable in tectonic strain release (King, Nason, & Tocher, 1973). We thus hypothesize that, similarly to the existence of different modes of fault slip, different modes of fault growth may exist. It is however challenging to distinguish by field observations if growth was seismic or aseismic. Despite multi-disciplinary efforts to study factors that control fault angles, no concept that differentiates between modes of fault growth has been established. One reason is that tackling this problem in a computational study requires a combination of challenging ingredients: i) self consistent long-term stress buildup that allows for a realistic fault zone setting due to spontaneous fault growth; ii) dynamic pressure; iii) earthquake dynamics; iv) adaptive time stepping due to the large difference in timescales (hundreds of years for fault evolution to milliseconds for rupture events); v) a laboratory based friction formulation (Dieterich, 1979, 1981; Ruina, 1983); vi) (visco)-elasto-plastic rheology.

Initial efforts in that direction were undertaken by the development of the seismo-thermo-mechanical (STM) modeling approach (van Dinther, Gerya, Dalguer, Corbi, et al., 2013; van Dinther, Gerya, Dalguer, Mai, et al., 2013). This approach extended the geodynamic approach, whose strength is the simulation of self consistent evolving fault zones on geological time-scales and that addresses large deformations on lithospheric length-scales. STM modeling implements inertia and a purely rate-dependent friction formulation to simulate fault slip events and growth along spontaneous rupture paths. To resolve both seismic and aseismic deformation, STM includes adaptive time stepping and an invariant continuum-based rate-and state-dependent friction formulation (RSF) (Herrendörfer, Gerya, & van Dinther, 2018). The current 2-D STM-RSF code simulates and resolves all stages of an earthquake cycle with realistic rupture properties in a visco-elasto-plastic compressible continuum with RSF. This includes seismic slip rates and rupture speeds at which shear and pressure waves are generated that interact with the dynamic rupture (Herrendörfer et al., 2018). The STM-RSF tool allows to study the combined full spectrum of long-term fault growth in relation to short-term rupture propagation. Here, for the first time we use this tool to study fault evolution.

In this study we investigate the process of fault growth and shed light on the role of seismic rupture during fault evolution by using the STM-RSF framework. We simulate these processes taking into account substantially different timescales and realistic rock properties. We identify for the first time two distinctly different modes of fault growth that can be distinguished by knowing only few measurable quantities: fault angle, angle of the maximum principal stress direction in the far-field and static friction coefficient of the host rock. Our presented results are insensitive to physical parameter changes and converge with numerical grid size.

The applied methodology can help assessing whether a fault formed seismically or aseismically. Furthermore we give an explanation for the typically observed fault bends in strike slip faults.

2 Methods

We present the main ingredients of the applied STM-RSF modeling approach (Herrendörfer et al., 2018) in section 2.1. We introduce the model setup and parameters in section 2.2.

2.1 Seismo-thermo-mechanical modeling with rate-and state-dependent friction

The 2-D problem we solve for is the conservation of mass:

$$\rho \frac{\partial v_i}{\partial x_i} = -\frac{D\rho}{Dt}, \tag{4}$$

and the conservation of momentum:

$$\frac{\partial \tau_{ij}}{\partial x_j} - \frac{\partial P}{\partial x_i} = \rho \frac{D v_i}{Dt} - \rho g_i, \tag{5}$$

where ρ denotes density, $\frac{D}{Dt}$ is the material time derivative, i and j are coordinate indices, x_i and x_j represent spatial coordinates, v_i is velocity, P is the dynamic pressure, g_i is gravity and τ_{ij} denotes the deviatoric stress tensor given as:

$$\tau_{ij} = \sigma_{ij} + \delta_{ij} P, \tag{6}$$

with σ_{ij} being the Cauchy stress tensor and δ_{ij} being the Kronecker delta. Dynamic pressure P is given by the mean stress:

$$P = -\frac{\sigma_{kk}}{3}, \qquad \text{with } k = 1, 2, 3, \tag{7}$$

where P is positive under compression. Computing the dynamic pressure as a solution of the continuity and momentum equations is especially crucial to obtain correct angles of forming faults that differ from a constant Roscoe angle (Buiter, 2012; Buiter et al., 2016; Kaus, 2010). Because our simulation represents a compressive state of stress, i.e. $\sigma_1 > \sigma_2$ and we ignore dilation, i.e. ψ=0, the four potential fracture surface orientations predicted by the Arthur angle (equation 3) reduce to: $\alpha_1 = 45°-(\varphi/4)$ and $\alpha_2 = -45°+(\varphi/4)$ (conjugate). Thus, the second pair of tensile fracture angles extinguishes. We assume a compressible medium with a compressibility defined via the bulk modulus K as:

$$\frac{D\rho}{Dt} = \frac{\rho}{K} \frac{DP}{Dt}. \tag{8}$$

This material is furthermore restricted to a visco-elasto-plastic rheology, in which, due to the choice of the initial viscosity value, the material essentially behaves as elasto-plastic (section 2.2). Damage representing the reduction of elastic moduli during deformation is neglected for reasons of simplicity. A constitutive relationship, which links deviatoric stresses τ_{ij} and deviatoric strain rates $\dot{\varepsilon}'_{ij}$ according to Gerya and Yuen (2007):

$$\dot{\varepsilon}'_{ij} = \frac{1}{2G}\frac{\overset{\triangledown}{D}\tau_{ij}}{Dt} + \frac{1}{2\eta}\tau_{ij} + \dot{\varepsilon}'_{II(plastic)}\frac{\tau_{ij}}{\tau_{II}}, \tag{9}$$

where G is the shear modulus, $\frac{\overset{\triangledown}{D}}{Dt}$ denotes the co-rotational time derivative, η is the effective ductile viscosity, $\dot{\varepsilon}'_{II(plastic)}$ is the second invariant of the deviatoric plastic strain rate and $\tau_{II} = \sqrt{{\tau_{xx}}^2 + {\tau_{yy}}^2}$ is the second invariant of the deviatoric stress tensor. Irreversible deformation can occur everywhere and spontaneously localizes into a shear band or fault zone of finite thickness, whose location and orientation are allowed to change through time. We use the yield function F to define the onset of plastic deformation by the yield criterion $F = 0$. The yield function is governed by a Drucker-Prager (Drucker & Prager, 1952) plastic yield function:

$$F = \tau_{II} - \sigma_{yield}, \quad \sigma_{yield} = \mu_l(1-\lambda)P + C, \tag{10}$$

where μ_l is the local friction coefficient, C denotes cohesion (residual shear strength) and λ is the pore fluid pressure factor and σ_{yield} is the pressure-dependent scalar material yield strength. We assume C=0 MPa, as typically done in RSF-modeling. This choice is explained in section 4.3. The scalars P and τ_{II} used in this approach are independent of the coordinate system and are able to adapt to spontaneous fault evolution. In contrast, in classical seismic cycle simulations fault strength is evaluated using normal stress σ_n and shear stress τ_s on a predefined, invariant fault.

The invariant reformulation of the classical RSF formalism according to Herrendörfer et al. (2018), in which we assume that $\sigma_{yield} = \tau_{II}$ and thus, $F = 0$, reads as:

$$\tau_{II} = \sigma_{yield} = \mu_l(1-\lambda)P = a\ P\ \text{arcsinh}\left[\frac{V_\text{p}}{2V_0}\exp\left(\frac{\mu_0 + b\ln\frac{\theta V_0}{L}}{a}\right)\right](1-\lambda), \tag{11}$$

where a and b are laboratory-based, empirical RSF values, L is the RSF characteristic slip distance and V_0 is an arbitrary reference slip velocity (Lapusta & Barbot, 2012). μ_0 is the reference static friction coefficient, θ denotes the evolving state variable with the aging evolution law

$$\frac{d\theta}{dt} = 1 - \frac{V_\text{p}\theta}{L}, \tag{12}$$

and V_p is the plastic slip rate defined by

$$V_\text{p} = 2\dot{\varepsilon}'_{II(p)}D, \tag{13}$$

where D denotes the thickness of the fault zone in the continuous host rock, which here is defined as $D = \Delta x$, where Δx is the numerical grid size. We use this approximation because in classical applications of plasticity the deformation localizes to within 1-2 grid cells (e.g. Lavier, Buck, & Poliakov, 2000; van Dinther, Gerya, Dalguer, Corbi, et al., 2013). However, this formulation makes the problem grid-size dependent. We demonstrate in section 3.4 that this grid-size dependence does not impact our conclusions. The relationship between slip rate and plastic strain rate may need a physics-based redefinition if deformation is distributed within more than a grid cell during the localization process toward a mature fault zone. This problem will be addressed in a future study in detail.

To solve the governing equations we use a 2-D numerical technique with an implicit, conservative finite-differences scheme on a fully staggered grid combined with the marker-in-cell technique (Gerya & Yuen, 2003, 2007). All details of the numerical technique that comprise the STM-RSF code can be found in Herrendörfer et al. (2018).

2.2 Model setup

The model setup represents a generic case to study the evolution of a fault zone. It is a 2-D plane strain model, in which the fault zone propagates as a mode II crack. The initial experimental geometry, together with the Dirichlet v_x-velocity boundary conditions applied in opposite directions at the top and bottom boundaries, represents a dextral strike slip zone (Fig. 1).

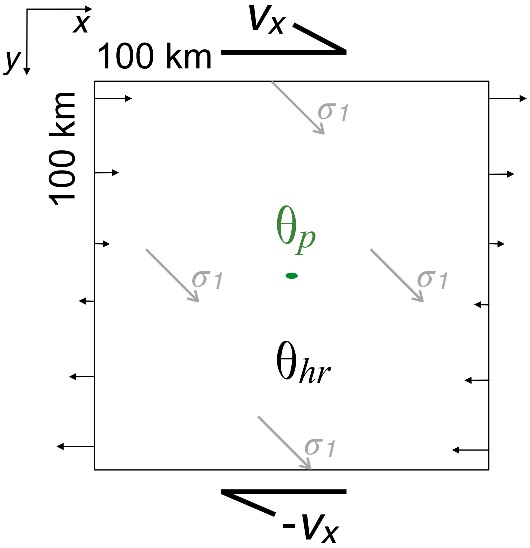

Figure 1. Model setup of the dextral inplane strike slip simulation. Box of size 100 km x 100 km with 401 x 401 nodes in x- and y-direction, respectively (grid resolution of 250 m). Bold black arrows show direction of Dirichlet v_x-velocity boundary conditions applied in opposite direction: $v_x = \pm 1.0 \cdot 10^{-9}$ m/s $= \pm 3.15$ cm/yr. At left and right boundaries Neumann boundary conditions for v_x are prescribed. The vertical velocity v_y is set to zero at all boundaries. The initial state θ_p is perturbed in an area of an elliptical shape (green) of twice the grid step size in x-direction ($2\Delta x$), by setting it ~ 403 times lower compared to that in the surrounding host rock. Gray arrow marks direction of initial σ_1-direction.

In such a dextral shear experiment the maximum compressive stress σ_1 is initially oriented at an angle of 45° to the imposed shear direction (e.g. Meyer, Kaus, & Passchier, 2017), indicated by the gray arrow in Fig. 1. We apply a weak perturbation in the center of the model, which will be the locus of stress concentration and thus the starting point of spontaneous fault growth. RSF- and material-parameters were adopted from Herrendörfer et al. (2018). Values for these parameters (Table 1) are largely in accordance with Lapusta, Rice, Ben-Zion, and Zheng (2000) with differences in the choice of V_0, μ_0 and the initial mean stress P_B. Following the proposition of Herrendörfer et al. (2018) we interpret V_0 as loading slip rate. Combination of elevated fluid pressure, found in a wide area surrounding fault zones (Hardebeck & Hauksson, 1999), and mean low permeability in the crust (Manning & Ingebritsen, 1999) result in fluid overpressuring above hydrostatic values ($\lambda > 0.4$) and approaching lithostatic values ($\lambda \sim 1.0$) (R. H. Sibson & Rowland, 2003), which reduces the effective lithostatic pressure and as a conse-

Table 1. RSF and material parameters

Parameters	Symbol	Value
Shear modulus	G	30 GPa
Bulk modulus	K	50 GPa
Density	ρ	2700 kg/m^3
Shear wave speed	c_s	3.3 km/s
Effective viscosity	η	$5{\cdot}10^{26}$ Pa s
Initial mean stress (pressure)	P_B	5 MPa
Gravity	g_i	0 m/s^2
Static friction coefficient	μ_0	0.2
Reference slip velocity	V_0	$2{\cdot}10^{-9}$ m/s = 6.3 cm/yr
Characteristic slip distance	L	0.0075 m
RSF direct effect	a	0.011
RSF evolution effect	b	0.018
Initial state		
Host rock	θ_{hr}	$\frac{L}{V_0}\exp(5)$ s $\approx$ 17.64 years
Perturbation	θ_p	$\frac{L}{V_0}\exp(-1)$ s $\approx$ 0.04 years

quence reduces the frictional sliding resistance of the crustal material. This agrees with the notion that water during sliding experiments decreases the coefficient of friction (Kohlstedt, Evans, & Mackwell, 1995). Hence, we choose $\lambda \sim 0.67$, which yields a lower effective friction $\mu_0 = 0.2$ with respect to Byerlee friction of 0.6. The initial pressure $P_B =$ 5 MPa is an effective quantity that is lowered due to pore fluid pressure P_f and is related to the initial lithostatic pressure $P_{B_{\text{lith}}}$ as:

$$P_B = (P_{B_{\text{lith}}} - P_f) = P_{B_{\text{lith}}}(1 - \lambda). \tag{14}$$

Thus, $P_{B_{\text{lith}}} = 15.2$ MPa, which is equivalent to a depth of 572 m, representing the upper crust. To confirm that our conclusions concerning fault angles hold true in case of an absent pore fluid pressure (i.e. $\lambda = 0$) or if we simulate at greater crustal depth, we investigate the role of μ_0 and P_B in section 3.5.

Note that Newtonian viscosity is constant and linear during these simulations which, for simplicity, ignore any non-linear effects of temperature and strain rate on the viscous rheology typically adopted in geodynamic models (Herrendörfer et al., 2018). This effective viscosity is very high ($5{\cdot}10^{26}$ Pa s), which results in a mainly elasto-plastic material behavior.

3 Results

In the reference model, we observe two successive stages of fault growth (stages S1 and S2) with slip velocities of distinctly different magnitudes (Fig. 2). In the following we analyze these different stages in terms of fault angle, stress orientation, slip rate and earthquake dynamics. The local dynamic friction coefficient μ_l (equations 10 and 11) and the dynamic σ_1-direction are scalar quantities that vary both in space and time. For both faulting stages μ_l and σ_1-direction are systematically measured at the current position of the fault tip (Fig. [4]). The fault tip is defined here as the point of maximum slip velocity. Within a square of size 1 km x 1 km that surrounds the current global maximum of the local friction value $\mu_{l_{\max}}$ (green filled square in Fig. [4]), the friction values that fulfill $\mu_l \geq \xi\ \mu_{l_{\max}}$ with $\xi = 0.5, 0.95, 0.99$, are chosen and averaged. Here ξ represents different percentiles to spatially sample data at different locations surrounding $\mu_{l_{\max}}$. From averaging we obtain the friction value μ_l^{av} at the fault tip. The σ_1-direction is averaged at the same points and thus referred to as σ_1^{av}.

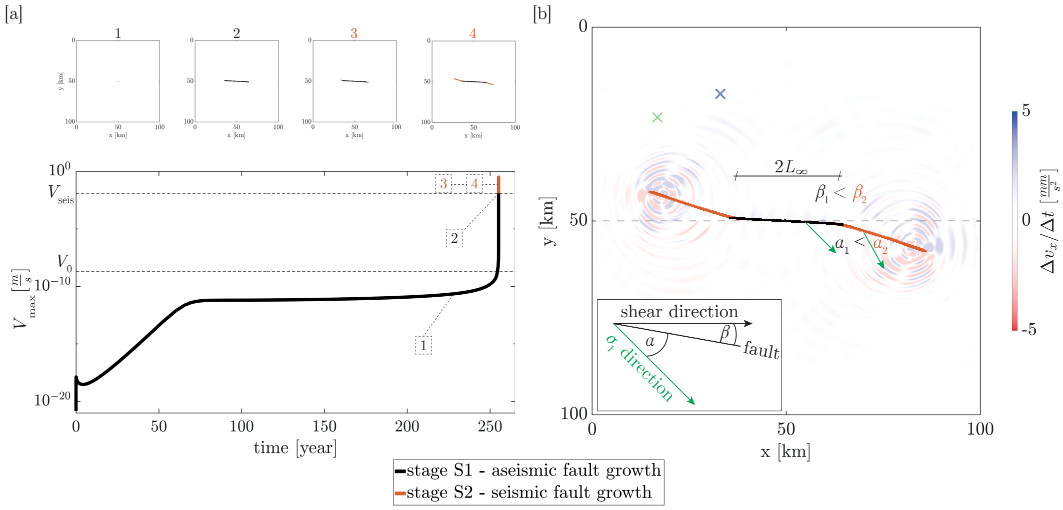

Figure 2. Two stages of fault growth with distinctly different slip velocities. The two faulting stages are indicated by color. [a]: Top panel: Four numbered snapshots of plastic strain ($\varepsilon_p > 10^{-4}$). Bottom panel: Maximum slip velocity versus time in years. V_0 and V_{seis} are indicated. V_{seis} is the threshold slip velocity that separates seismic and aseismic faulting stages. Numbers indicate the stages of fault evolution shown in the snapshots of the top panel. [b]: Modeled fault pattern indicated by plastic strain ($\varepsilon_p > 10^{-4}$) at the end of the simulation overlain with seismic waves indicated by horizontal acceleration at this instant. L_∞ indicates the nucleation length, α is the angle between the two fault segments and the σ_1-direction (green arrow in the inset), $\alpha_1 < \alpha_2$. β is the angle between the horizontal E-W shearing direction (0°, black dashed line) and the respective fault segment, $\beta_1 < \beta_2$. Green and blue crosses mark accelerometer locations for seismogram in Fig. [10].

3.1 Stage 1 - Aseismic fault growth

At the beginning of the first stage of faulting (S1), the entire model is elastically loaded due to the imposed shearing at the upper and lower boundaries. In the first 70 years stresses concentrate at the boundary of the weak perturbation. During this initial localization process, the logarithm of the global maximum slip velocity $\log(V_{\text{max}})$ increases linearly (Fig. [2a]). At the end of the localization process two new shear surfaces emerge and the growth rate of slip velocity decreases. One shear band with orientation close to the E-W-oriented shear direction and one conjugate shear band (not shown) develop in the model center at the location of the weak perturbation. The E-W shear band is favored due to the elliptical shape of the weak perturbation and the imposed shear direction. This shear band starts to grow at both sides of the perturbation in +x and -x direction at an angle $\beta_1 = \pm 3.5°$ (Fig. [2b] and [4a]). Since right and left shear bands grow in simultaneous and symmetric fashion, we focus on the right branch (i.e. positive x- and y-sector) in the following. This branch reaches a length of 7.8 km after 254.5 years, at which point $V_{\max}$ has approached the reference slip velocity V_0 at the propagating shear band tip (Fig. [2a]). Interestingly, while $V_{max} < V_0$, $\mu_l^{\mathrm{av}}$and the orientation of σ_1^{av} are relatively constant in the entire model domain and remain close to their initial values (Fig. 3). Within the next 0.72 years, $V_{\max}$ increases 7 orders of magnitude while it is still in the aseismic range of slip velocities. The fault continues to grow at a constant angle β_1 in this aseismic fault growth stage. Simultaneously, the shear band localizes further to a 1 grid-step wide feature that now represents a localized fault strand with $\mu_l^{\mathrm{av}}$and the orientation of σ_1^{av} starting to increase slightly (Fig. 3). This is caused by the direct effect of the RSF formulation, which represents the immediate increase of friction and stresses to an increase in V_{p}. The observed elevated slip velocities thus lead to $\mu_l^{\mathrm{av}} = 0.26$ and $\sigma_1^{\mathrm{av}} = 45.4°$ at the fault tip (Fig. [4b]). Moreover, the σ_1-direction decreases north of the fault (counter-clockwise rotation) and increases south of the fault (clockwise rotation). We note here that the increase of friction (at the fault tip) and the slight rotation of stresses (north and south of the fault) occurs only very close to the propagating fault (Fig. [4b]). Far from the fault, in the rest of the model domain, both quantities remain very close to their initial values. We define the angle α as the difference be-

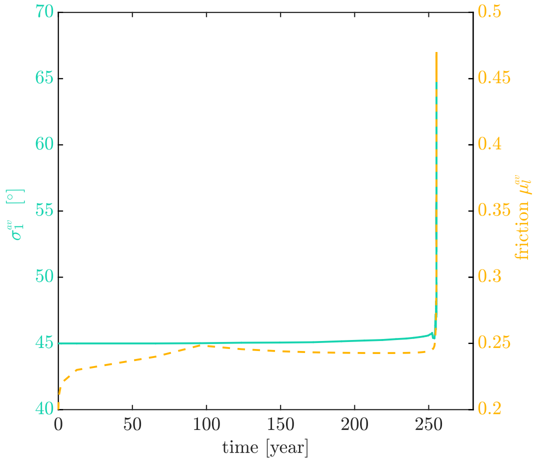

Figure 3. Maximum friction $\mu_l^{\mathrm{av}}$and σ_1^{av}, which are averaged in the area around the propagating fault tip, versus time in years.

tween the σ_1-direction and the fault angle β according to $\alpha = \sigma_1 - \beta$. Combining the averaged maximum local friction coefficient μ_l^{av}, the σ_1^{av}-direction and β_1, we are able to plot the angular-frictional relation for stage S1. The result is consistent with the Arthur angle prediction (black square in Fig. [5a]). The end of stage S1 is reached as V_{max} transitions to seismic slip velocities $V_{\mathrm{seis}} = 0.012$ m/s, which is determined by Rubin and Ampuero (2005) as the slip velocity at which the radiation of seismic waves produces stress changes on the fault comparable to those induced by the direct effect of RSF:

$$V_{\mathrm{seis}} = \frac{2aPc_s}{G}. \tag{15}$$

At this point the right fault segment attains a length of 14.5 km and is straight with $\beta_1 = \pm 3.5^\circ$, which means that the entire fault is 29 km long.

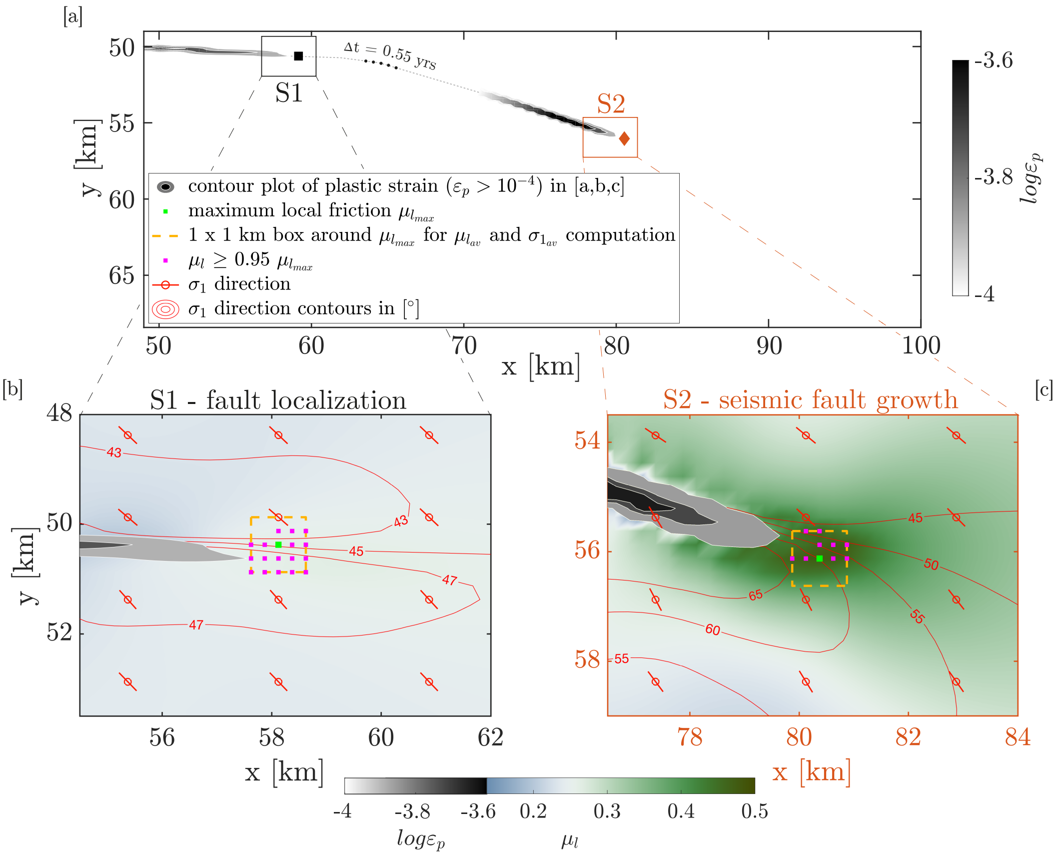

Figure 4. Evolution of friction μ_l and σ_1-direction for faulting stages S1 and S2. [a]: Contour plot showing plastic strain in gray colors with white contours at two distinct points in time. Plot is cropped to first quadrant of the model domain. Location where friction and stress directions are picked are indicated by black square (S1) and orange diamond (S2). The evolution in between these two points in time (duration of 0.55 years) is displayed schematically by a gray dashed line and black dots. [b] and [c] are snapshot zooms of the friction distribution, representative for stage S1 and S2, respectively. The fault itself is plotted as plastic strain ε_p in gray colors with white contours. Orange box (1 km x 1 km) contains the global maximum of the friction coefficient, $\mu_{l_{\max}}$, in its center (green filled square). Magenta filled squares in this box mark the values that are used to compute μ_l^{av}(0.26 and 0.46 for S1 and S2, respectively) and σ_1^{av} (45.4° and 56.3° for S1 and S2, respectively) according to the 95% percentile (explanation at beginning of section 3). In addition, $\mu_{l_{av}}$ and σ_1^{av} are computed with the 50% and the 99% percentile. The average of these three values of $\mu_l^{\mathrm{av}}$and α, calculated from $\sigma_1^{av} - \beta$, are then plotted in Fig. [5a]. Red lines with circle indicate pointwise local direction of σ_1, red contour lines represent the distribution of σ_1 orientations. Rotation of the σ_1-direction in stage S2 is evident.

3.2 Stage 2 - Seismic fault growth

After the aseismic fault growth stage, a dynamic slip event nucleates at the location of the initial weak seed and the fault produces an earthquake. The length of left and right fault segments when V_{seis} is exceeded agrees well with the theoretical estimate of the nucleation size L_∞ of 14 km, which depends on RSF- and material-parameters and normal stress as Rubin and Ampuero (2005). We adapt this formulation using P instead of normal stress as done in invariant-RSF and explained before equation 11:

$$L_\infty = \frac{2}{\pi}\frac{GbL}{(b-a)^2P(1-\nu)}, \tag{16}$$

The factor 2 difference between the length of the entire fault and the theoretical L_∞ stems from the thickness of the fault that is ∼2 times the grid size Δx. This doubles the apparent L in our simulation. Because simultaneously to the nucleation of the dynamic event, V_{max} exceeds the seismic slip velocity threshold V_{seis} (Fig. [2a]), we refer to this dynamic phase as seismic fault growth stage (S2).

It takes $\sim 5\ s$ from the nucleation of the event in the center until two rupture fronts reach the fault tips that were formed in stage S1. During this process, V_{max} increases approximately by a factor of 5 (from 0.012 m/s to 0.058 m/s), which results in the generation of shear and pressure waves as shown in the video in the supplementary material and in the repository for this publication (Preuss, Herrendörfer, Gerya, Ampuero, & van Dinther, 2018). As the rupture reaches the old fault tip of stage S1, the fault starts to bend and the fault angle β increases. The bending lasts 6 seconds and afterwards the fault propagates seismically at an angle $\beta_2 = \pm 18.7°$ (Fig. [2b] and [4a,c]). This dynamic fault growth angle β_2 remains stable throughout the rest of the simulation. Due to the direct effect of RSF, elevated slip velocities additionally induce an increase of the friction coefficient up to $\mu_{l_2}^{av} = 0.47$ and a rotation of the average σ_1-direction to a maximum value of $\sigma_{1_2}^{av} = 65°$ (Fig. [3]). A clear global maximum of $\mu_l^{\mathrm{av}}$is observed at the fault tip while it drops to a minimum of 0.006 within the most mature, central part of the fault and the σ_1-direction is clearly elevated in the vicinity of the fault and ahead of the fault tip (Fig. [4c]). Due to the simultaneous jump of σ_1-direction and friction value at the fault tip, the dynamically formed fault follows the theory of the Arthur angle when applied to the elevated dynamic quantities (β_2, $\mu_{l_2}^{av}$, $\sigma_{1_2}^{av}$). Thus, the fault angle of S2 plots very close to the Arthur failure curve in Fig. [5a].

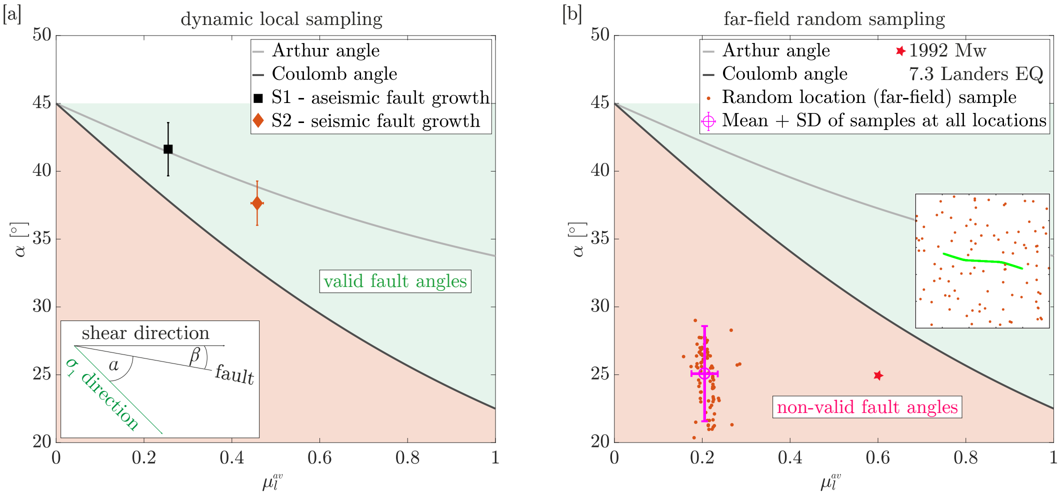

Figure 5. Relation between friction $\mu_{l_k}^{av}$ and fault angle α. Angle α calculates as $\alpha_k = \sigma_{1_k}^{av} - \beta_k$, where $k = 1, 2$ indicates the respective faulting stage. β is measured relative to the E-W shearing direction, explanation in inset of left panel. [a]: Taking dynamic local values into account. S1 and S2 plot close to the Arthur angle function and lie within the valid range of fault angles (green shaded polygon). Given errorbars indicate the standard deviation when using different percentiles (0.5, 0.95, 0.99) for calculating $\mu_{l_k}^{av}$ and $\sigma_{1_k}^{av}$, respectively. The angle α_k is subjected to an additional measuring error that stems from measuring β_k. This error is taken into account and was added to the vertical errorbars. [b]: Taking far-field random (dynamic or static) samples into account. Orange dots indicate data from 100 randomly chosen locations. Their location around the green fault is visualized within inset in [b]. Pink data represent mean and standard deviation taking into account data from all grid points. We only consider seismically formed fault S2 with an angle of $\beta_2 = 18.7°$. Averaged σ_1-direction in the entire model is $44.1°$, thus, $\alpha = \sigma_1 - \beta_2 \sim 25.4°$. μ_l is 0.21 on average in the entire model. Data lie within the non-valid range of fault angles (red shaded polygon). Red star indicates the 1992 Landers earthquake (section 4.1.1). Here we assume a static friction of 0.6.

In the following 27.4 s of the dynamic event the evolving fault extends by 22.3 km and the maximum slip velocity on the fault reaches 0.83 m/s before the fault hits the side boundary. We stop the simulation at the moment when the fault segment has reached a length of 36.8 km to impede boundary interaction. The rupture event shows a crack like rupture behavior during the entire simulation, such that at every point in time the fault continues to slip (Fig. [6b]). At the beginning of stage S2 the amount of slip increase at the propagating fault tip is slightly lower than in the model center and at the end of stage S2 it is slightly higher than in the most mature fault section. As the fault transitions to stage S2, shortly after the dynamic event has nucleated in the model center, we observe a transient increase of the rupture velocity V_r up to 1 km/s. As the rupture reaches the tip formed during stage S1 it decelerates rapidly and V_r decreases due to more energy needed to break the intact rock ahead of the fault tip (Fig. [6a]). In the following, V_r increases towards the end of the simulation in an unsteady, oscillatory manner. This reflects numerical noise due to the rupture cutting through the numerical grid, leading to inaccuracies in simulations and measurements. This behavior is also visible in the slip contours in Fig. [6b]). However, V_r never reaches the speed of around 2.5 km/s that is observed on a predefined weak fault zone in an otherwise similar model (Herrendörfer et al., 2018), because in our model energy is consumed by breaking intact rock.

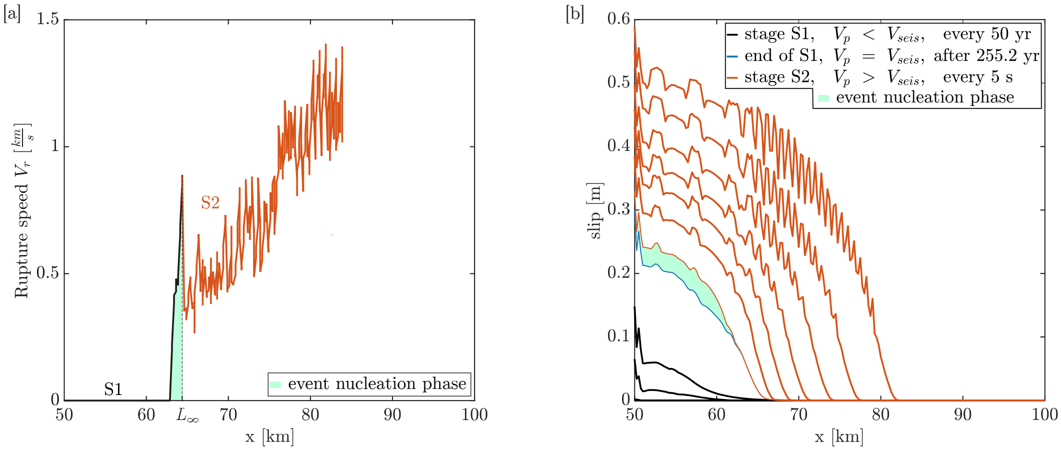

Figure 6. Rupture and slip properties during stage S2. [a]: Half length of rupture $R_\mathrm{l}/2$ and speed of the rupture front V_r along the x-axis starting from the center of the model at x = 50 km. Event nucleation phase is indicated in turquoise, the nucleation length L_∞ is indicated and marks the transition from stage S1 (gray polygon) to stage S2 (red polygon). [b]: Slip contours, plotted at regular times, whose interval depends on V_p as indicated in the legend. End of stage S1 and the successive event nucleation phase are indicated. Stage S1 is represented by 5 lines, which add up to a total of 250 yr. However, during the initial localization phase no slip is accumulated and thus, only 3 lines are visible.

3.3 Far-field sampling and effects

In nature it is not possible to obtain both dynamic and local measures of an angular-frictional relation as we can do in simulations. The reason is that: i) Stress and friction measurements are not feasible proximal to a propagating fault tip; ii) dynamic measurements of these quantities during fault propagation cannot be obtained (explained in discussion section 4.1.2).

To demonstrate that wrong conclusions can be drawn from usually available far-field measurements, we imitate an off-fault borehole measurement by taking 100 samples of μ_l and σ_1-direction at random locations in our model. Next, we sample each grid point of the model domain for both quantities and individually compute mean and standard deviation of their sums, respectively.

The result, considering the seismically formed fault (S2), shows that random location measurements as well as averaged measurements from all locations plot far from Arthur angle and Coulomb angle curves (Fig. [5b]). They lie within a sector of the plot that can be labeled *non-valid fault angles*, because these data points do not fulfill the Andersonian faulting theory. The reason for this behavior is that the global average of the σ_1-direction remains at 44.1° and friction at $\mu = 0.205$. Both values are very close to their initial values. These far-field values do not change between dynamic and static phases. Data points that lie at $\alpha \approx 30°$ were sampled close to or inside the fault zone but not at the fault tip.

3.4 Grid size dependence

In this section we present the effects of grid size changes on fault angles. We increase the numerical resolution by decreasing the grid size from 500 m to 125 m. The reference model has the intermediate resolution of Δx = 250 m. Variations of fault angles lie within the errorbars. In the low resolution model with Δx = 500 m, the fault angle during stage S1 is $\beta_1 = 0°$ and the resolution is too low to resolve the fault inclination. The angle β is influenced by the numerical resolution (Fig. [7b]). Faults become steeper with increasing resolution during both faulting stages. This is because the finer the grid the better the simulation resolves the peak slip velocity of the rupture in the process zone L_b defined by Rubin and Ampuero (2005) as it approaches the fault tip formed during S1. The process zone L_b during quasi-static rupture is 2.9 km in our simulation and is resolved with 11 grid points. During dynamic rupture propagation it decreases as shown by Herrendörfer et al. (2018). A higher V_p induces higher friction and higher stresses in the undeformed matrix at the beginning of stage S2 and hence, the fault gets steeper. In contrast, the angle α, which is used especially to assess the optimality of fault angles, is only affected marginally by resolution changes (Fig. [7a]). Thus, our main findings concerning the fault angles remain well-founded.

The presented numerical sensitivity analysis indicates that our results are valid for $\Delta\mathrm{x} \leq 250$ m at which resolution we can distinguish two different stages of fault growth. Additionally, the conclusions we draw from our results, based on stress rotations and frictional increase during time-dependent fault formation are valid for aseismic and seismic fault growth.

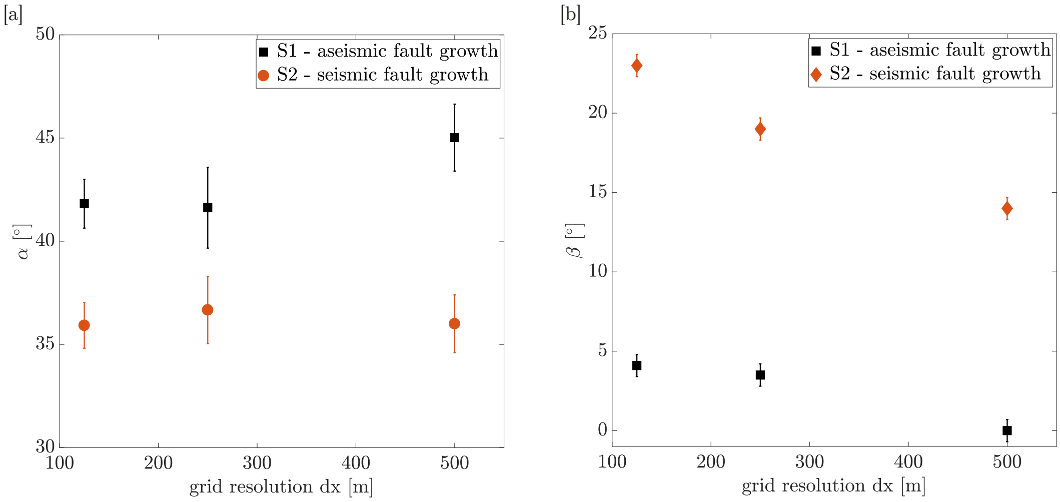

Figure 7. Relation between grid resolution and fault angles. [a]: Grid resolution in meter versus angle α. Colors indicate different faulting stages. Grid size has a minor effect on the measured angles. Errorbars indicate the standard deviation when using different percentiles (0.5, 0.95, 0.99) for calculating σ_1^{av} at the fault tip. The uncertainty in the measurement of β is added to this error as it is contained in the calculation of α. [b]: Grid resolution in meter versus angle β. Increasing grid size results in increasing fault angles. Errorbars indicate the uncertainty in the measurement of β.

3.5 Effect of RSF parameters

In this section we present the effects of changes of modeling parameters on fault angles. We systematically increase and decrease all RSF parameters by 30% to analyze the effect on fault angles. We are mainly interested in the impact of parameter changes on the angle α. Changing parameters a, b, L, μ_0, P, θ and V_0 individually does not change the relation we observe in the reference model between angle α and maximum averaged friction value at the fault tip μ_l^{av}. All simulations plot close to the Arthur angle line. Variations lie within the measurement error described in Fig. [5a] and [7a]. Thus, all simulations result in an Andersonian type of faulting for both faulting stages and our main message, that fault orientation depends on whether fault growth is seismic or aseismic, holds true. We aimed at keeping all numerical parameters between the individual simulations constant. The only exceptions are the cases of 30% higher a and 30% lower b, for which we had to increase the domain size to 350 km x 350 km and 1000 km x 1000 km, respectively. The reason is that by either increasing a or decreasing b, the nucleation size L_∞ increases dramatically, since it depends quadratically on (b-a) in equation 3.2. This effect is strongest for a change in a, where a rather small change of 30% increases the nucleation size to 100 km. Interestingly, changing a has the highest impact on β. We discussed this in the beginning of section 4 by introducing equation 17. As a consequence, changing parameter a causes an alteration of fault angles of 1.3° and 6° for stages S1 and S2, respectively (with respect to the reference model). The change of μ_0 increases or decreases angle β in a similar manner. In contrast, changing L, P, θ or V_0 has only minor influence on the total fault angle β.

We also modeled fault growth at different depths by increasing and decreasing pressure P by a factor of 2 and 4 ($P = 1.25$, 2.5, 10 and 20 MPa, respectively). These changes of P influence the nucleation size of the fault and thus the length of faults generated in phase S1 and S2, but not the angle α. This suggests that our results about fault angles can be expanded to different depths of the brittle crust.

An increase of μ_0 to Byerlee friction of 0.6, which can be interpreted as the absence of pore fluid pressure (i.e. $\lambda = 0$), increases the angle β by 6° (S1) and 2.8° (S2) with respect to the reference model. However, as in all other presented models, the angle of the seismically formed fault lies in between Coulomb and Arthur fault angle (void black symbols in Fig. 8).

To simulate pure aseismic fault growth we increase the value of L by a factor of 10. This increases L_∞ by an equal factor of 10. Hence, this simulation is reduced to a fault localization phase and an aseismic fault growth stage (S1), while seismic fault growth is prevented. The resulting fault angle is in agreement with the faulting stage S1 of the reference model (black filled symbols in Fig. 8). Additionally, the fault angle β_1 corresponds to the fault angle that emerges when RSF is off and the yield strength of the medium is computed with a pressure dependent Drucker-Prager yielding criterion using a constant static friction coefficient. The angular-frictional relation between α and μ_l^{av} does not change if the initial friction coefficient of host rock and weak seed are changed independently or simultaneously in these models without RSF.

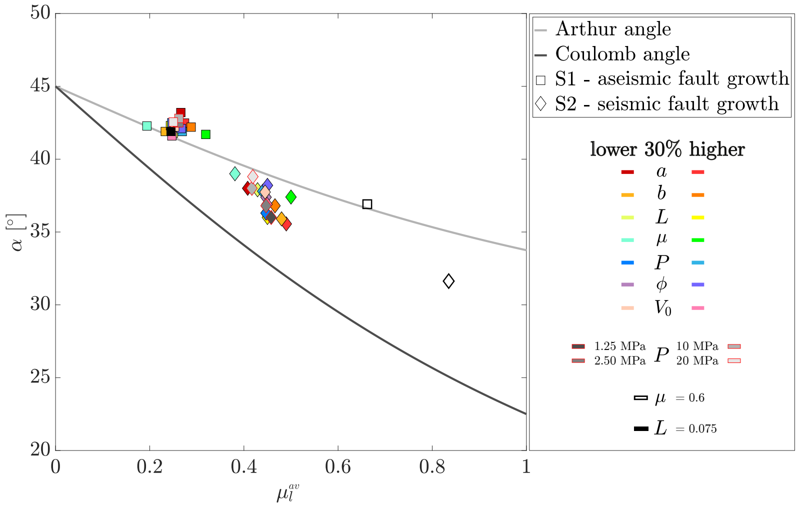

Figure 8. Relation between friction μ_l^{av} and fault angle α for a variety of RSF parameter changes. Colorful symbols represent + 30% and - 30% changes of all RSF parameters. Gray symbols with red contour show changes of Pressure by a factor of 1/2, 1/4, 2 and 4, respectively. Void black symbols represent the case of Byerlee friction $\mu = 0.6$. Black filled symbols represent aseismic fault growth with $L = 0.075$ m.

4 Discussion

We identified two fault growth modes that can be distinguished by both their angle β relative to the reference E-W shearing direction and by their angle α relative to the σ_1-direction. The transition between the two modes occurs as the slip velocity reaches V_{seis} and each side of the fault (i.e. half of the entire fault) measures a length corresponding to L_∞. At this moment, a dynamic rupture event nucleates on the fault and as $V_{\max}$ keeps rising, further fault growth is driven at a steeper angle. This steeper angle β suggests the corresponding fault formed seismically.

Furthermore, we observe that the fault-tip stress plays an important role in forming new fault surface and an alteration of the stress field surrounding the fault leads to an increase in mean stress and stress rotations there. This was similarly reported by Ando, Shaw, and Scholz (e.g. 2009); Faulkner, Mitchell, Healy, and Heap (e.g. 2006); Mitchell and Faulkner (e.g. 2009). We extend their view by adding that the *time-dependent value of the stresses* and the *time-dependent friction coefficient* ahead of the fault tip need to be taken into account when assessing fault angles of forming faults. This finding supports our first hypothesis. When taking into account time-dependent and local quantities of the angular-frictional relation, both aseismic and seismic fault growth mode produce faults at an Arthur angle. Formation at an Arthur angle is also observed for Riedel shear localization on a frictional interface using dynamic rupture simulations (Xu & Ben-Zion, 2013).

Our simulations show that dynamic and local friction coefficient and stress orientations increase temporally when a propagating fault tip reaches a given point (Fig. [3,4]). The location of the peak friction value $\mu_{l_2}^{\text{av}}$ at the fault tip moves and the spatial offset between $\mu_{l_2}^{\text{av}}$ and the peak slip velocity $V_{\max}$ is constant at around 2.5 km during stage S2. We conclude that the increased fault angle is slip velocity induced and is due to the slip-rate dependence of the friction value in the RSF formulation. The peak friction $\mu_{l_2}^{\text{av}}$ is then given as:

$$\mu_{l_2}^{\text{av}} = \mu_{\text{pre}} + a \cdot \log\left(\frac{V_{\max}}{V_{\text{pre}}}\right), \tag{17}$$

where μ_{pre} and V_{pre} are the friction and slip velocity before the arrival of the rupture front. This estimate of $\mu_{l_2}^{\text{av}}$ arises from the fact that the acceleration of slip at a given point is so fast that θ does not have time to evolve. The stress increase ahead of the rupture is due to dynamic stress transfer from the slipping region.

In addition, we present a way to assess whether a natural fault formed seismically or aseismically by mimicking far-field measurements in our model:

1. A fault formed *aseismically* when far-field friction and the angle α between fault and far-field σ_1-direction suggest a *valid, Andersonian fault.*
2. A fault formed *seismically* when far-field friction and the angle α between fault and far-field σ_1-direction suggest a *non-valid, non-Andersonian fault.*

This distinction is possible, because an aseismically formed fault always results in a valid Arthur fault angle, independent on location and time of the measurement. In contrast, a seismically formed fault can only correctly be assessed as Andersonian fault when considering local dynamic (time-dependent) friction and stress orientation at the fault tip. We note that these implications are only true if the far-field stresses are constant on the timescale considered for fault assessment. Long-term, large-scale tectonic re-arrangements can alter stress orientations. However, since most stress measurements are obtained near-term, this issue becomes minor.

We pursue this line of reasoning in the following section by considering the 1992 Landers earthquake.

4.1 Comparison to natural examples

4.1.1 1992 Landers earthquake

The 1992 Mw 7.3 Landers earthquake on the Landers-Mojave fault is believed to have formed a new fault (Nur, Ron, & Scottti, 1989) at high angle ($\sim 47°$) to the main San Andreas fault (Fig. [9], and detailed explanation in the appendix B). Comparing it to the *far-field* stress field (σ_1 direction of N10°E), this fault would have a low value $\alpha \approx 25°$ and it would thus plot in the non-valid fault angle range in Fig. [5b], assuming a static friction of 0.6. On the basis of our model, a high value for β and a low far-field value for α suggest that the fault may have formed in the seismic mode. This supports the suggestion of Nur et al. (1993), that the Landers-Mojave fault is an emerging seismogenic fault that hosted six Mw ≥ 5 earthquakes in the last 50 years (appendix B). If, however, we use the *local* stresses (in 10 km vicinity of the fault) to assess the fault orientation, it follows $\alpha \approx 40°$. This brings the fault in the valid range of fault angles and thus, makes it an Andersonian fault. Here we assume that the local stresses did not reorganize or rotate back after fault formation since no measurements during fault formation are available. In addition, this suggests, that under the current stress field the fault is prone to break again. We emphasize that this statement can only be made if the present day local stress field is equivalent to the measured (old) local stress field. Yet, if this is not true, and, if stresses rotated, faults become critically aligned or misaligned with stresses and can get abandoned such that new faults are formed (Scholz et al., 2010) or old structures are reactivated. This explains the fan of splay faults surrounding fault tips (Perrin, Manighetti, & Gaudemer, 2016) where some faults get abandoned as the fault continues to grow and new splay faults are formed. Consequently, we propose that a fault at an angle $\gtrsim 25^\circ$ to the parent fault has formed seismically. This is only true if fault growth was not affected by surrounding structural heterogeneities.

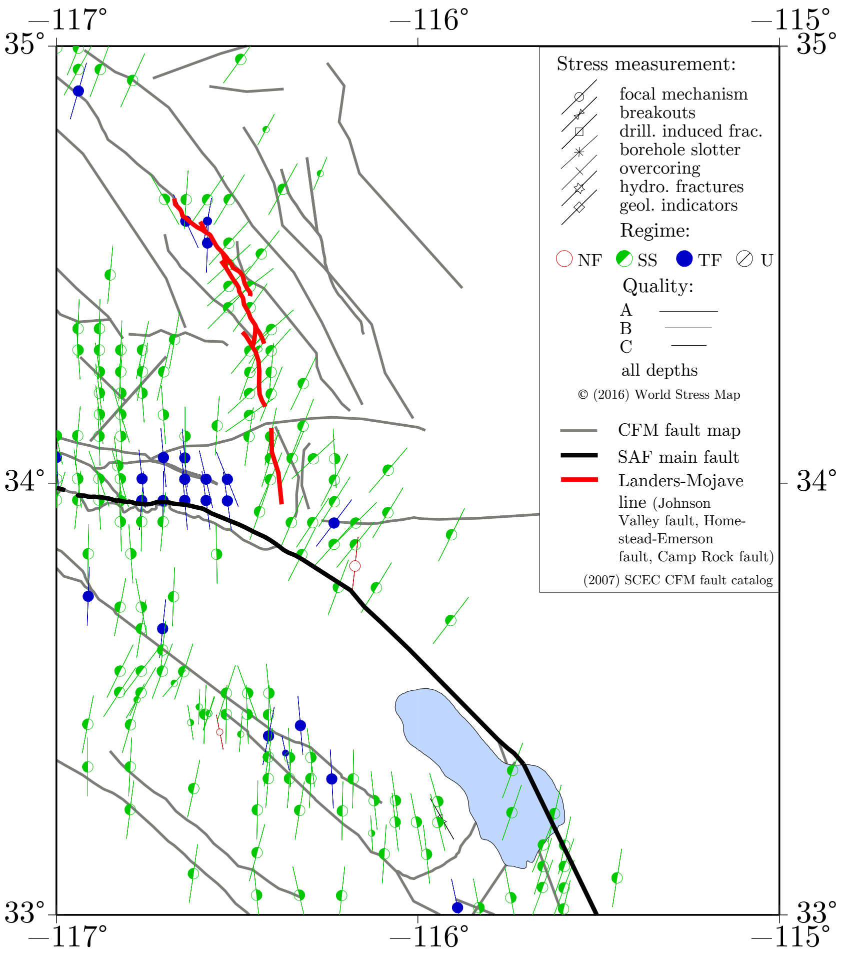

Figure 9. Stress map of the eastern California shear zone from World Stress Map (Heidbach et al., 2018) combined with Community Fault Model (CFM) fault catalog from Southern California Earthquake Center (Plesch et al., 2017, 2007). Local data points in green, blue and red represent σ_1 orientations obtained from focal mechanisms. SS-strike slip, TF-thrust faulting, NF-normal faulting. Red lines represent Landers-Mojave fault line (Johnson Valley fault, Homestead Valley fault, Camp Rock-Emerson fault). Black line marks San Andreas main fault. Gray lines are the before 1992 mapped faults. Colored symbols indicate stress measurements.

4.1.2 Sampling friction angles and stress orientations

Stress measurements like well bore breakouts, drilling-induced fractures and in-situ stress measurements (overcoring, hydraulic fracturing, borehole slotter) do not exist in immediate proximity (< 1 km) to the fault and earthquake focal mechanisms, on the other hand, are not suitable to determine friction coefficients (pers. communication: Heidbach et al., 2018). An exception to the lack of in-situ stress measurements is the SAFOD drilling into the San Andreas fault at Parkfield (Hickman & Zoback, 2004; M. Zoback, Hickman, & Ellsworth, 2010). However, even in this location it is not possible to measure μ and σ_1-direction during the dynamic rupture propagation. Especially, it is not possible to sample data during fault growth as the sampling location would have to move with the propagating fault tip. Furthermore, SAFOD is clearly not located at the current fault tip of a San Andreas fault segment. The stress and friction data we obtain in nature are static ones compared to the timescale of an earthquake and they are subject to a large error. Furthermore, they can be interpreted as reflecting a far-field behavior of the stress field, although they are obtained at a definite location. In this paper we show how these static far-field values can be used to assess whether a fault formed seismically or aseismically.

4.1.3 Relation to fault bends and kinks

Many faults in nature have kinks or bends (e.g. Biasi & Wesnousky, 2017, and references therein). Our results provide a possible explanation for fault bends. When a fault transitions from aseismic to seismic fault growth as slip velocities increase, the fault line will bend, change its direction and become steeper. Bending at an average angle of $\pm$ 17° from the San Andreas fault deviate only slightly from the bend angle of $\pm$ 15.2° we observe between stages S1 and S2 (Ando et al., 2009). This provides an explanation for fault bends in addition to the influence of structural characteristics on the fault angle. As pointed out in section 4.2, we expect that in a 3-D simulation the seismic growth phase can stop spontaneously. Subsequently it can be followed by aseismic slip, leading to alternating episodes of seismic and aseismic fault growth, and thus a sequence of fault bends. The spacing between fault bends was shown to be $\sim$ 18 km for continental strike-slip faults and controlled by the thickness of the seismogenic crust (Klinger, 2010).

4.1.4 Implication for fault maturation in a weak material

We simulate fault growth in a weak material (low initial friction and low initial state contrast). The stress field before fault growth is homogenous and without disturbances in the host rock. This facilitates fault growth in contrast to the case of material with a higher strength or existing stress heterogeneities. Thus, a single seismic event can form a several tens of km long fault due to the high potential strain energy in the vicinity of the fault. The latter is possible because of elevated stresses at the fault tip. In the case of weak material, enough energy is available to feed fault growth. We expect that prevailing heterogeneity in structure or stresses might challenge this behavior. Indeed, in simulations with a higher state of the host rock in combination with a non-optimally oriented initial fault we observe additional fault branching, which increases stress field alteration and reduces the length of formed faults per event. This observations has, however, no influence on the findings of this study and will be discussed in a follow-up study. This study aimed at studying fault growth in the most simple setup.

4.1.5 Relation to slip spectrum

The second hypothesis of this paper is that different modes of fault growth may exist, similarly to the existence of different modes of fault slip. Natural faults generate a wide slip spectrum ranging from dynamic, coseismic slip to fault creep (e.g. parts of the Haiyuan Fault in China (Jolivet et al., 2013)). Additionally, decades of observations demonstrate that small, moderate, and large earthquakes occur on creeping shallow crustal faults around the world (Harris, 2017; Lindsey, Fialko, Bock, Sandwell, & Bilham, 2014). Evidence that seismic and aseismic slip coincide on the same fault segment is rare, however few observations exist: Four seismically inactive patches have different locations after the Izmit (before the Düzce) and after the Düzce mainshock (Bohnhoff, Ickrath, & Dresen, 2016), which can be interpreted as shifting of aseismic fault patches along the fault. Furthermore, two of these inactive fault patches are co-located or coincide with the maxima of the coseismic slip (Bohnhoff et al., 2016). Areas of coseismic slip coincide with fault areas that are otherwise aseismic on the Calaveras fault , as shown for the 1979 Coyote Lake and the 1984 Morgan Hill earthquake (Oppenheimer, Bakun, & Lindh, 1990). Additionally, an 8 month slow slip event triggered progressive nucleation of the 2014 Chile megathrust, that broke both frictional asperities and surrounding conditionally stable areas, which, before, hosted slow slip and superimposed seismic signals (Socquet et al., 2017). The above observations are supported by recent modeling studies in which slip can change from slow slip to fast rupture events on the same fault segment (Noda & Lapusta, 2013; Veedu & Barbot, 2016). Thus, faults generate a wide slip spectrum. In this study we additional show that fault growth is equally accompanied by varying slip velocities. We furthermore show that, as a result of these varying slip velocities, two fault growth modes exist.

4.1.6 Seismic wave analysis

We record generated seismic waves at two stations whose location is displayed in Fig. [2b]. The seismogram in Fig. [10a] plots the time series of time derivatives of v_x- and v_y-velocities. The accelerometer at location 1 records the E-W component first, while the N-S ground acceleration is first recorded at location 2. Taking into account that the start of recording of the seismogram is right at the beginning of stage S2, the approximate onset of all arrivals between 5 s and 10 s agrees well with the theoretical P-wave speed c_p of 5.6 km/s (using a P-wave/S-wave ratio $c_p/\ c_s$ of 1.7) and the averaged distance of the two locations from the event nucleation point of ∼40 km, yielding ∼7.1 s travel time. The dominant frequency content of the waveforms is below 2 Hz (Fig. [10b]). This value is higher than in the case of a rupture event on a predefined fault in a similar model, in which the dominant frequency content is below 0.5 Hz (Fig. 9 in Herrendörfer et al. (2018)).

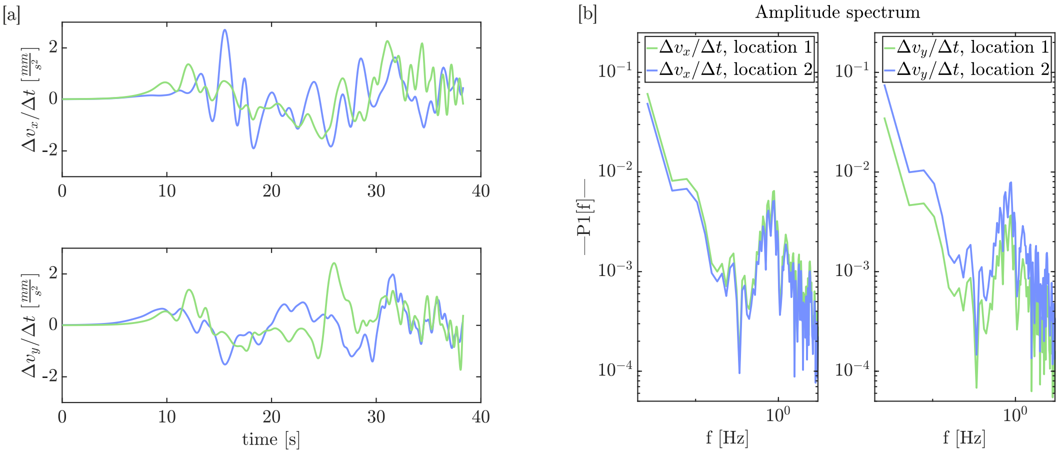

Figure 10. Seismic wave properties during stage S2. [a]: Time series of time derivatives of E-W v_x (upper panel) and N-S v_y (lower panel) velocities at two locations as indicated with the correspondingly colored crosses in Fig [2b]. The two accelerometers are located at equivalent positions as in Herrendörfer et al. (2018). [b]: Amplitude spectra of the waveforms in [a].

4.2 Modeling limitations and uncertainties

In nature, fault growth is a three-dimensional process. With our presented 2-D plane strain model we neglect the third dimension and instead assume perfectly vertical fault surfaces. This is valid in a first order sense, however, various natural strike slip faults can have changing dip angles with depth (e.g. Ross et al., 2017). Another drawback of our 2-D simulations is the finiteness of the seismogenic depth. This limits the stress concentration at the fault tip, which in turn limits the spatial extent of plasticity outside the main fault (Ampuero & Mao, 2017) and the energy available for a dynamic rupture to keep growing (Weng & Yang, 2017). Potentially, in 3-D the dynamic rupture would stop spontaneously after some propagation distance larger than the seismogenic depth. At much longer time scales, viscous relaxation below the crust could counteract this effect of seismogenic depth (Ampuero & Mao, 2017). Another effect ignored is the stress concentration at the base of the seismogenic zone induced by deeper fault creep. This allows earthquakes to start at depth while the rest of the fault at shallower depth still has low stress, giving a low depth-average apparent fault strength. Additionally, changes of frictional parameters and material parameters (e.g. shear modulus) with plastic strain are not taken into account in our simulations.

The grid size dependence of the angle β (section 3.4) is a limitation of our model that we will address in a future study. We aim at proposing and testing one alternative invariant continuum-based RSF formulation for fault width D, such that during the strain localization phase D adapts dynamically as a function of evolving material parameters.

4.3 Role of cohesion

In our simulations we assume the material has zero residual strength (C=0 MPa), as typically assumed in RSF-modeling. This is justified by numerical tests from Herrendörfer (2018, section 7.2.2), which showed that a cohesionless fault embedded in a cohesive host rock produces the same results as a simulation with a cohesionless fault embedded in a cohesionless host rock. Additionally, Herrendörfer (2018, section 7.2.2) demonstrated that cohesion applied along the fault does not change the overall earthquake cycle behavior apart from the fact that more time is required to generate the first earthquake. Herrendörfer (2018, section 7.2.2) follows from these tests that adding cohesion has essentially the same effect as increasing the reference static friction μ_0 by an equivalent amount (Herrendörfer, 2018, section 7.2.2). To confirm that cohesion has no influence on fault angles during rapid fault growth we present a simulation with a cohesive host rock in section 3.5. We note that a nonzero cohesion in the host rock does not change fault angles and thus, will not change our results and conclusions. Furthermore, the higher initial state in the host rock compared to the weak inclusion can be considered to be equivalent to a higher cohesion there.

5 Conclusions

We systematically studied the process of spontaneous fault growth using a model that allows for the spontaneous evolution of a fault governed by an invariant rate-and state-dependent friction formulation. Our two hypotheses are: 1) When assessing fault angles, local instantaneous near-tip stress field and friction coefficient need to be taken into account during all phases of fault formation. 2) We propose that, similarly to the existence of slow and fast modes of fault slip, seismic and aseismic modes of fault growth may exist. Our findings confirm these hypotheses and comprise:

1. Two end member fault growth modes are distinguished in a generic model of a strike-slip fault zone, which are *aseismic* and *seismic* fault growth. After an early stage of shear band localization faults grow aseismically until they reach the nucleation size of a dynamic event. As the event nucleates, the slip velocity increases and the growing fault transitions to a seismic propagation mode. The result is a greater strike angle of the growing fault, which leads to a fault bend. This finding supports our second hypothesis.
2. The increase of the total fault angle at the transition between the aseismic and seismic faulting stage is induced by slip rate. It is due to the slip-rate dependence of the friction value in the RSF formulation. Seismic fault growth causes significantly elevated dynamic stresses, stress orientations and friction coefficient at and ahead of the propagating fault tip. These local dynamic quantities cause the increase in fault angle. This finding supports both our hypotheses.
3. With respect to the far-field stress field, aseismic fault growth agrees with Andersonian faulting, while the seismic fault growth stage does not agree with it. However, in relation to local and dynamic quantities, both fault growth modes obey the Andersonian faulting theory. It follows that all faults form as predicted by the failure criterion of Mohr-Coulomb, because they grow according to the state of stress prevailing at the time of genesis. Consequently, the assessment of the optimality of fault angles requires the consideration of local near-tip stress field and friction

coefficient in a dynamic sense, i.e. during the phase of fault formation. This finding further supports our first hypothesis.

4. We show that the main conclusions are not affected by numerical and physical parameters.
5. The four previous points suggest that seismically formed faults can be distinguished from aseismically formed faults in two ways in nature:
   (a) By comparing them to far-field stress orientations: An aseismically formed fault will be predicted as an Andersonian fault, while a seismically formed fault will be predicted as a non-Andersonian fault. The reason is that local stress field and friction value are marginally altered during aseismic fault growth, but they are significantly altered during the seismic stage of propagation. However, the far-field stress field and far-field samples of the friction value are not affected by local fault growth. This conclusion underlies the assumption that the far-field stresses are constant on the timescale considered for fault assessment. That is mostly valid as stress measurements are obtained near-term. The above statement is supported by the analysis of the stress field in the region of the 1992 Landers earthquake on the Landers-Mojave fault where only the near-fault stresses have rotated.

   (b) By comparing them to the shearing direction: In relation to the shearing direction seismically formed faults are steeper than aseismically formed faults. We propose that a fault at an angle $\gtrsim 25°$ to the parent fault has formed in seismic mode. We obtain this value from the analysis of the stress field and fault angle of the Landers-Mojave fault line that formed seismically near-term to the 1992 Landers earthquake. We make this statement under the assumption that fault growth was not effected by surrounding structural heterogeneities.
6. The fault orientation could be used to predict the dynamic stress field during seismic fault formation, which is otherwise not measurable.
7. Our results have implications for big strike slip systems as e.g. the San Andreas fault. The stress field surrounding mature fault zones is often misaligned with existing faults. This is due to a combination of the following factors: reorientation of the stress field during fault formation, long-term reorientation of stresses due to strain accumulation, structural complexity, e.g. induced by nearby faults and general heterogeneity of stresses on a local to far-field scale. The misalignment of

the stress field with existing faults facilitates the reactivation of inactive and potentially blind or unknown fault branches and can additionally cause formation of new faults. Our approach gives an indication how such new faults can grow and at which angle.

A Mohr-Coulomb failure criteria

Upper crustal faults obey Mohr-Coulomb failure criteria (Norris & Toy, 2014; R. Sibson et al., 2011; R. H. Sibson, 1994) as set out by M. Anderson (1942) and Byerlee (1978). Application of this theory to natural stress states forms the basis of the classical and widely accepted conceptual model for conjugate fault patterns (Healy et al., 2015) and Andersonian faulting (Anderson, 1905). Andersonian faulting is a standard rule of thumb in assessing optimally oriented faults (Fang & Dunham, 2013) and largely validated by the World Stress Map Project (Heidbach et al., 2018; Scholz et al., 2010). Typically, to visualize a materials state of stress and proximity to failure, the Mohr stress space is used (Fig. A.1). The red failure line represents the Coulomb fracture criterion which states that a shear fracture occurs if the yield strength of a rock is reached, i.e. the rock cannot sustain any increase in shear stress or second stress invariant (Zang & Stephansson, 2010). The slope of the failure line is controlled by the angle of internal friction φ which relates to the friction coefficient μ:

$$\mu = \tan\varphi. \tag{A.1}$$

The maximum compressive principal stress σ_1 and the minimum compressive principal stress σ_2 (in 2-D) of an intact rock are found where shear stresses $\tau_{xy} = \tau_{yx} = 0$ (or $\tau_{II} = 0$, Fig. A.1). The angle at which the failure plane is oriented to that maximum principal stress direction σ_1 is α, as explained in section 1. According to the theory, newly formed subsidiary fractures within intact isotropic crust in a wrench stress regime (vertical stress component equals intermediate principal stress: $\sigma_v = \sigma_2$) should be vertically dipping and lie at ±30° to the orientation of the maximum principal stress σ_1 (R. Sibson et al., 2011), assuming a friction coefficient of μ=0.58. Consequently, R-Riedel shears, the most prominent subsidiary fractures, develop at an acute angle, typically $10-20°$ to the main fault (Twiss & Moores, 1992). However, natural faults reveal a contradicting behavior: A population of 47 worldwide crustal faults with rigorous different length scales and different slip modes (Perrin, Manighetti, & Gaudemer, 2016) yields, that angular bins of maximum splay angles have a large variety of splay angles following an uni-

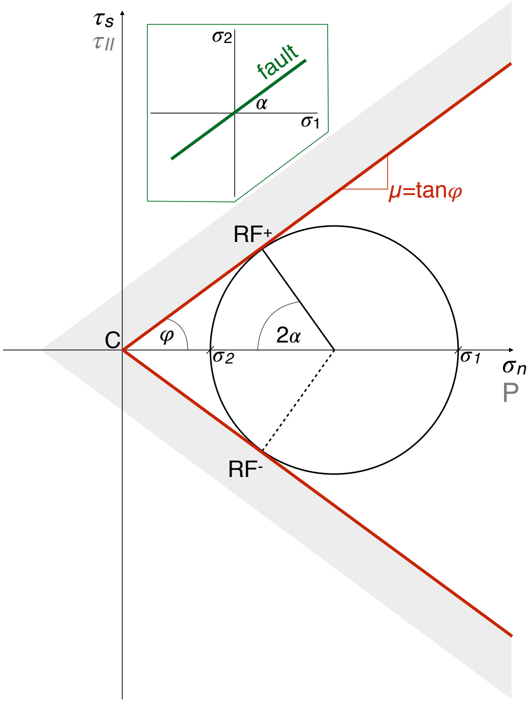

Figure A.1. Drucker-Prager yielding criterion in Mohr stress space, gray shaded area is the failure regime of rock, parameters in gray denote notation typically used in geodynamics. RF^+ and RF^- denote stress state where rock failure occurs. Inset: orientation of fault in relation to principal stresses σ_1 and σ_2 in the physical space in 2-D.

modal distribution with a peak at $]30-50]^\circ$ (Fig. A.2). Observations can lead to the quick conclusion that, in particular cases, Andersonian faulting is not valid and corresponding faults are considered 'non-Andersonian'. Hence, the Coulomb-Mohr criterion fails to address problems regarding first order splay faults (Scholz et al., 2010), such as mentioned large variation in fault angles in nature. In line with this, large displacement strike slip faults commonly lie at far higher angles (often $> 45^\circ$) to far-field σ_1-trajectories and are distinctly non-Andersonian (Hardebeck & Michael, 2004; R. Sibson et al., 2011; R. H. Sibson, 1990; Townend & Zoback, 2004, and references therein). This behavior is not too surprising, since misoriented faults whose positioning is not conducive to rupture are also common (Fletcher et al., 2016). When the primary fault becomes critically misaligned with the principal stresses or inefficient, formation of a new fault (splay fault) on an optimum plane for faulting, is favored (Fattaruso, Cooke, Dorsey, & Housen, 2016; Scholz et al., 2010).

It follows that vertical, low-displacement strike slip faults at Andersonian orientations are possibly newly formed structures in the contemporary stress field (R. Sibson et al., 2011). Consequently, to assess fault orientations, the stress field at the time of fault formation must be considered. The crux is, the stress field at the very same time of fault formation is unknown in nature.

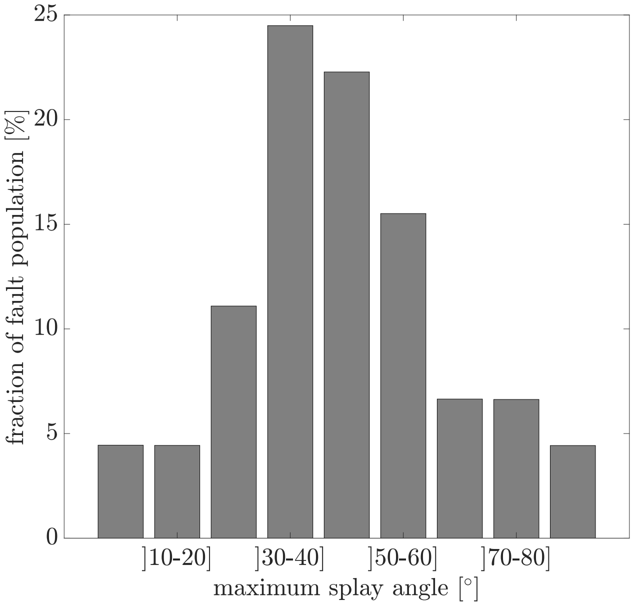

Figure A.2. Distribution of maximum splay fault angles relative to average parent fault strike (data from Perrin, Manighetti, and Gaudemer (2016))

Additionally, the faulting theory, connecting stress directions and fault angles, must be subjected to a spatial aspect: Near-fault failure may occur even if the far-field stress state is not conducive to continued propagation of a fault branch (Andrews, 2005). Modeling studies showed that not far-field, but local (near tip) stresses control splay fault angles (Du & Aydin, 1995) and dynamic effects strongly distort elastically predicted stress fields near rapidly propagating crack tips (Poliakov et al., 2002). Combination of field observations, laboratory experiments and numerical modeling yield that stress rotation occurs within the fractured damage zone surrounding faults (Faulkner et al., 2006; Mitchell & Faulkner, 2009). This holds in particular, for unfavorably oriented 'weak' faults (Faulkner et al., 2006), i.e. mature, large displacement strike slip faults such as the San Andreas fault (Carpenter, Marone, & Saffer, 2011; R. H. Sibson, 1990).

B 1992 Landers earthquake on the Landers-Mojave fault line

We consider here the example of the 1992 Mw 7.3 Landers earthquake, which occurred off the main San Andreas fault. Precisely, it nucleated on the Johnson Valley fault and ruptured two more fault segments, the Homestead Valley fault and the Camp Rock-Emerson fault (Plesch et al., 2007). However, at the time of the event these faults were not known, which led Nur et al. (1989) to conclude, even before the event, that a new set of faults was in the process of forming. This being a controversial hypothesis at the time, considering arguments about fault growth, about heterogeneity of crustal stresses that were proposed to be caused by a ductile middle crust and the believe that block rotations in California must be clockwise (Nur et al., 1993). Their hypothesis was based on observations and the fact that the well-developed N-W oriented strike slip faults in the region (gray lines in Fig. 9) were mechanically unfavorably oriented with respect to the maximum tectonic compressional stresses σ_1 (Nur et al., 1993; Stein, King, & Lin, 1992; M. D. Zoback, 1991; M. D. Zoback et al., 1987). Thus, a new, favorably oriented fault formed whose existence is proven and well accepted today. Scholz et al. (2010) strengthen this view by stating that 'stress directions are homogeneous over southern California, but they are heterogeneous at small to medium scales. Much of that heterogeneity results from perturbations produced by the major faults (Hardebeck & Hauksson, 1999; Scholz, 2000; Scholz et al., 2010) and would not have existed prior to the formation of those faults (the period in which we apply the assumption of homogeneity).' The new fault is aligned at a high angle ($\sim 47°$) to the main San Andreas fault.

Fig. 9 shows the stress field in the Landers region. It illustrates two aspects: i) The stress orientations in the direct vicinity of the Landers-Mojave fault (in red) deviate from the overall, far-field stress pattern in the region (N25°E vs. N10°E). ii) The fact that the N15°W strike of the Landers-Mojave fault line is at low angle to the far-field but at higher angle to the local stresses confirms that the fault formed seismically as demonstrated in section 4.

In addition, i) affirms the hypothesis that fault formation changes the stress field adjacent to the formed fault and that far-field stresses were potentially not affected by the formation of the new fault network as they had a similar orientation before 1992. This would be true even if the fault was a blind fault and formed not due to the 1992 seismic event, but before. This example furthermore validates our statement that when assessing fault angles to understand fault growth, both temporal and local variations of stresses are crucial.

C Online repository

A video showing the temporal evolution of the fault and also the generation of shear and pressure waves is in the repository of this paper (Preuss et al., 2018) and can be found under this link.

Acknowledgments

The repository cited in the references (Preuss et al., 2018) contains an executable, with which the reference model can be rerun. Figures 2 - 10 of this paper can thus be reproduced. This project has received funding from the European Union's Horizon 2020 research and innovation program under the Marie Sklodowska-Curie grant agreement 642029 - ITN CREEP. Jean Paul Ampuero acknowledges support through the project FAULTS_R_GEMS ANR-17-CE31-0008 of the French National Research Agency (ANR). We thank ... to be added later.

References

Ampuero, J. P., & Mao, X. (2017). Upper limit on damage zone thickness controlled by seismogenic depth. *Fault Zone Dynamic Processes: Evolution of Fault Properties During Seismic Rupture*, *227*, 243. doi: 10.1002/9781119156895.ch13

Anderson, E. M. . (1905). The Dynamics of Faulting. *Transactions of the Edinburgh Geological Society*, *V8*(February 2010), 387–402. doi: 10.1080/10942911003754718

Ando, R., Shaw, B. E., & Scholz, C. H. (2009). Quantifying natural fault geometry: Statistical of splay fault angles. *Bulletin of the Seismological Society of America*, *99*(1), 389–395. doi: 10.1785/0120080942

Andrews, D. J. (2005). Rupture dynamics with energy loss outside the slip zone. *Journal of Geophysical Research: Solid Earth*, *110*(1), 1–14. doi: 10.1029/2004JB003191

Arthur, J. R. F., Dunstan, T., Al-Ani, Q., & Assadi, A. (1977). Plastic deformation and failure in granular media. *Géotechnique*, *27*(1), 53–74.

Aydin, A., & Berryman, J. G. (2010). Analysis of the growth of strike-slip faults using effective medium theory. *Journal of Structural Geology*, *32*(11), 1629–1642. Retrieved from `http://dx.doi.org/10.1016/j.jsg.2009.11.007` doi: 10.1016/j.jsg.2009.11.007

Ben-Zion, Y. (2008). Collective behavior of earthquakes and faults: Continuumdiscrete transitions, progressive evolutionary changes, and different dynamic regimes. *Reviews of Geophysics*, *46*, 1–70. doi: 10.1029/2008RG000260

Biasi, G. P., & Wesnousky, S. G. (2017). Bends and Ends of Surface Ruptures. *Bulletin of the Seismological Society of America*, *107*(6), 2543–2560. Retrieved from `http://pubs.geoscienceworld.org/bssa/ssa/bssa/article/107/6/2543/519320/Bends-and-Ends-of-Surface-RupturesBends-and-Ends` doi: 10.1785/0120160292

Bohnhoff, M., Ickrath, M., & Dresen, G. (2016). Seismicity distribution in conjunction with spatiotemporal variations of coseismic slip and postseismic creep along the combined 1999 Izmit-Düzce rupture. *Tectonophysics*, *686*, 132–145. Retrieved from `http://dx.doi.org/10.1016/j.tecto.2016.07.029` doi: 10.1016/j.tecto.2016.07.029

Buiter, S. J. H. (2012). A review of brittle compressional wedge models. *Tectonophysics*, *530-531*(0040), 1–17. Retrieved from `http://dx.doi.org/10.1016/j.tecto.2011.12.018` doi: 10.1016/j.tecto.2011.12.018

Buiter, S. J. H., Schreurs, G., Albertz, M., Gerya, T. V., Kaus, B., Landry, W., … Beaumont, C. (2016). Benchmarking numerical models of brittle thrust wedges. *Journal of Structural Geology*, *92*, 140–177. doi: 10.1016/j.jsg.2016.03.003

Bürgmann, R., Pollard, D. D., & Martel, S. J. (1994). Slip distributions on faults: effects of stress gradients, inelastic deformation, heterogeneous host-rock stiffness, and fault interaction. *Journal of Structural Geology*, *16*(12), 1675–1690. doi: 10.1016/0191-8141(94)90134-1

Byerlee, J. (1978). Friction of rocks. *Pure and Applied Geophysics PAGEOPH*, *116*(4-5), 615–626. doi: 10.1007/BF00876528

Carpenter, B. M., Marone, C., & Saffer, D. M. (2011). Weakness of the San Andreas Fault revealed by samples from the active fault zone. *Nature Geoscience*, *4*(4), 251–254. Retrieved from `http://dx.doi.org/10.1038/ngeo1089` doi: 10.1038/ngeo1089

Choi, E., & Petersen, K. D. (2015). Making Coulomb angle-oriented shear bands in numerical tectonic models. *Tectonophysics*, *657*, 94–101. Retrieved from `http://dx.doi.org/10.1016/j.tecto.2015.06.026` doi: 10.1016/j.tecto.2015.06.026

Cooke, M. (1997). Fracture localization along faults with spatially varying friction. *Journal of Geophysical Research*, *102*, 22425–22434.

Cowie, P. A., & Scholz, C. H. (1992a). Growth of faults by accumulation of seismic slip. *Journal of Geophysical Research*, *97*(B7), 11085. Retrieved from `http://doi.wiley.com/10.1029/92JB00586` doi: 10.1029/92JB00586

Cowie, P. A., & Scholz, C. H. (1992b). Physical explanation for the displacement-length relationship of faults using a post-yield fracture mechanics model. *Journal of Structural Geology*, *14*(10), 1133–1148. doi: 10.1016/0191-8141(92)90065-5

Dal Zilio, L., van Dinther, Y., Gerya, T. V., & Pranger, C. C. (2018). Seismic behaviour of mountain belts controlled by plate convergence rate. *Earth and Planetary Science Letters*, *482*, 81–92. Retrieved from `https://doi.org/10.1016/j.epsl.2017.10.053` doi: 10.1016/j.epsl.2017.10.053

Dieterich, J. H. (1979). Modeling of rock friction: 1. Experimental results and constituve equations. *Journal of geophysical research*, *84*(9), 2161–2168. Retrieved from `http://dx.doi.org/10.1007/BF00876539` doi: 10.1007/BF00876539

Dieterich, J. H. (1981). Constitutive Properties of Faults With Simulated Gouge. *Geophysical Monograph Series*, *24*, 103–120. Retrieved from `http://doi.wiley.com/10.1029/GM024p0103` doi: 10.1029/GM024p0103

Drucker, D. C., & Prager, W. (1952). Soil mechanics and plastic analysis or limit design. *Quarterly of Applied Mathematics*, *10*(2), 157–165. Retrieved from `http://www.ams.org/qam/1952-10-02/S0033-569X-1952-48291-2/` doi: 10.1090/qam/48291

Du, Y., & Aydin, A. (1995). Shear fracture patterns and connectivity at geometric complexities along strike-slip faults. *Journal of Geophysical Research*, *100*(95), 93–102.

Fang, Z., & Dunham, E. M. (2013). Additional shear resistance from fault roughness and stress levels on geometrically complex faults. *Journal of Geophysical Research: Solid Earth*, *118*(7), 3642–3654. doi: 10.1002/jgrb.50262

Fattaruso, L. A., Cooke, M. L., Dorsey, R. J., & Housen, B. A. (2016). Response of deformation patterns to reorganization of the southern San Andreas fault system since ca. 1.5Ma. *Tectonophysics*, *693*, 474–488. Retrieved from `http://linkinghub.elsevier.com/retrieve/pii/S0040195116301615` doi: 10.1016/j.tecto.2016.05.035

Faulkner, D. R., Mitchell, T. M., Healy, D., & Heap, M. J. (2006). Slip on 'weak' faults by the rotation of regional stress in the fracture damage zone. *Nature*, *444* (7121), 922–925. doi: 10.1038/nature05353

Fletcher, J. M., Oskin, M. E., & Teran, O. J. (2016). The role of a keystone fault in triggering the complex El Mayor-Cucapah earthquake rupture. *Nature Geoscience*, *9* (4), 303–307. doi: 10.1038/ngeo2660

Gerya, T., & Yuen, D. A. (2003). Characteristics-based marker-in-cell method with conservative finite-differences schemes for modeling geological flows with strongly variable transport properties. *Physics of the Earth and Planetary Interiors*, *140* (4), 293–318. doi: 10.1016/j.pepi.2003.09.006

Gerya, T., & Yuen, D. A. (2007). Robust characteristics method for modelling multiphase visco-elasto-plastic thermo-mechanical problems. *Physics of the Earth and Planetary Interiors*, *163* (1-4), 83–105. Retrieved from `http://linkinghub.elsevier.com/retrieve/pii/S0031920107000969` doi: 10.1016/j.pepi.2007.04.015

Hardebeck, J. L., & Hauksson, E. (1999). Role of fluids in faulting inferred from stress field signatures. *Science*, *285* (5425), 236–239. doi: 10.1126/science.285.5425.236

Hardebeck, J. L., & Michael, A. J. (2004). Stress orientations at intermediate angles to the San Andreas Fault, California. *Journal of Geophysical Research: Solid Earth*, *109* (11), 1–16. doi: 10.1029/2004JB003239

Harris, R. A. (2017). Large earthquakes and creeping faults. *Reviews of Geophysics*, *55* (1), 169–198. doi: 10.1002/2016RG000539

Healy, D., Blenkinsop, T. G., Timms, N. E., Meredith, P. G., Mitchell, T. M., & Cooke, M. L. (2015). Polymodal faulting: Time for a new angle on shear failure. *Journal of Structural Geology*, *80*, 57–71. Retrieved from `http://dx.doi.org/10.1016/j.jsg.2015.08.013` doi: 10.1016/j.jsg.2015.08.013

Heidbach, O., Rajabi, M., Cui, X., Fuchs, K., Müller, B., Reinecker, J., . . .

Zoback, M. (2018). The World Stress Map database release 2016: Crustal stress pattern across scales. *Tectonophysics*, *744* (July), 484–498. Retrieved from `https://doi.org/10.1016/j.tecto.2018.07.007` doi: 10.1016/j.tecto.2018.07.007

Herrendörfer, R. (2018). *Modeling of the slip spectrum along mature and spontaneously forming faults in a visco-elasto-plastic continuum* (Doctoral dissertation, ETH Zurich). doi: https://doi.org/10.3929/ethz-b-000304601

Herrendörfer, R., Gerya, T. V., & van Dinther, Y. (2018). An Invariant Rate- and State-Dependent Friction Formulation for Viscoeastoplastic Earthquake Cycle Simulations. *Journal of Geophysical Research: Solid Earth*, *123* (6), 5018–5051. doi: 10.1029/2017JB015225

Hickman, S., & Zoback, M. (2004). Stress orientations and magnitudes in the SAFOD pilot hole. *Geophysical Research Letters*, *31* (15), 13–16. doi: 10.1029/2004GL020043

Hirsch, P. B. (1975). *Work hardening In: The Physics of Metals 2. Defects* (P. B. Hirsch, Ed.). Cambridge University Press.

Ida, Y. (1974). Slow-moving deformation pulses along tectonic faults. *Physics of the Earth and Planetary Interiors*, *9* (4), 328–337. doi: 10.1016/0031-9201(74) 90060-0

Jolivet, R., Lasserre, C., Doin, M. P., Peltzer, G., Avouac, J. P., Sun, J., & Dailu, R. (2013). Spatio-temporal evolution of aseismic slip along the Haiyuan fault, China: Implications for fault frictional properties. *Earth and Planetary Science Letters*, *377-378*, 23–33. Retrieved from `http://dx.doi.org/10.1016/j.epsl.2013.07.020` doi: 10.1016/j.epsl.2013.07.020

Kaus, B. J. P. (2010). Factors that control the angle of shear bands in geodynamic numerical models of brittle deformation. *Tectonophysics*, *484* (1-4), 36–47. Retrieved from `http://dx.doi.org/10.1016/j.tecto.2009.08.042` doi: 10.1016/j.tecto.2009.08.042

Kim, W., Hong, T. K., Lee, J., & Taira, T. (2016). Seismicity and fault geometry of the San Andreas fault around Parkfield, California and their implications. *Tectonophysics*, *677-678*, 34–44. Retrieved from `http://dx.doi.org/10.1016/j.tecto.2016.03.038` doi: 10.1016/j.tecto.2016.03.038

King, Y. C., Nason, R. D., & Tocher, D. (1973). Kinematics of fault creep. *Philo-*

sophical Transactions of the Royal Society. Series A, Mathematical and Physical Sciences, *274*(1239), 355–360.

Klinger, Y. (2010). Relation between continental strike-slip earthquake segmentation and thickness of the crust. *Journal of Geophysical Research: Solid Earth*, *115*(7), 1–19. doi: 10.1029/2009JB006550

Kohlstedt, Evans, & Mackwell. (1995). Strength of the lithosphere: Constraints imposed by laboratory experiments. *Journal of the Franklin Institute*, *181*(6), 845–848. doi: 10.1016/S0016-0032(16)90156-X

Lapusta, N., & Barbot, S. (2012). *Models of earthquakes and aseismic slip based on laboratory-derived rate and state friction laws* (Vol. 661).

Lapusta, N., Rice, J. R., Ben-Zion, Y., & Zheng, G. (2000). Elastodynamic analysis for slow tectonic loading with spontaneous rupture episodes on faults with rate- and state-dependent friction. *Journal of Geophysical Research*, *105*, 23765. doi: 10.1029/2000JB900250

Lavier, L. L., Buck, W. R., & Poliakov, A. N. B. (2000). Factors controlling normal fault offset in an ideal brittle layer. *Journal of Geophysical Research*, *105*(B10), 23431. Retrieved from `http://www.agu.org/pubs/crossref/2000/2000JB900108.shtml` doi: 10.1029/2000JB900108

Lehner, F. K., Li, V. C., & Rice, J. R. (1981). Stress Diffusion Along Rupturing Plate Boundaries. *Journal of Geophysical Research*, *86*, 6155–6169.

Lindsey, E. O., Fialko, Y., Bock, Y., Sandwell, D. T., & Bilham, R. (2014). Localized and distributed creep along the southern San Andreas Fault. *Journal of Geophysical Research: Solid Earth*, *119*(10), 7909–7922. doi: 10.1002/2014JB011275

M. Anderson, E. (1942). The Dynamics of Faulting. *Trans. Edinburgh Geol. Soc.*, *8*.

Manighetti, I., Campillo, M., Sammis, C., Mai, P. M., & King, G. (2005). Evidence for self-similar, triangular slip distributions on earthquakes: Implications for earthquake and fault mechanics. *Journal of Geophysical Research: Solid Earth*, *110*(5), 1–25. doi: 10.1029/2004JB003174

Manighetti, I., King, G., & Sammis, C. G. (2004). The role of off-fault damage in the evolution of normal faults. *Earth and Planetary Science Letters*, *217*(3-4), 399–408. doi: 10.1016/S0012-821X(03)00601-0

Manighetti, I., King, G. C. P., & Gaudemer, Y. (2001). Slip accumulation and lateral propagation of active normal faults in Afar. *Journal of Geophysical Research*, *106*(B7), 13,613–667,696.

Manning, C. E., & Ingebritsen, S. E. (1999). Permeability Implications of the Continental of Geothermal Data Crust and Metamorphic Systems. *Reviews of Geophysics*, *37*(1), 127–150.

Meyer, S. E., Kaus, B., & Passchier, C. (2017). Development of branching brittle and ductile shear zones: A numerical study. *Geochemistry, Geophysics, Geosystems*. Retrieved from `http://doi.wiley.com/10.1002/2016GC006793` doi: 10.1002/2016GC006793

Mitchell, T. M., & Faulkner, D. R. (2009). The nature and origin of off-fault damage surrounding strike-slip fault zones with a wide range of displacements: A field study from the Atacama fault system, northern Chile. *Journal of Structural Geology*, *31*(8), 802–816. Retrieved from `http://dx.doi.org/10.1016/j.jsg.2009.05.002` doi: 10.1016/j.jsg.2009.05.002

Noda, H., & Lapusta, N. (2013). Stable creeping fault segments can become destructive as a result of dynamic weakening. *Nature*, *493*(7433), 518–521. Retrieved from `http://www.ncbi.nlm.nih.gov/pubmed/23302798` doi: 10.1038/nature11703

Norris, R. J., & Toy, V. G. (2014). Continental transforms: A view from the Alpine Fault. *Journal of Structural Geology*, *64*, 3–31. Retrieved from `http://dx.doi.org/10.1016/j.jsg.2014.03.003` doi: 10.1016/j.jsg.2014.03.003

Nur, A., Ron, H., & Beroza, G. (1993). *Landers-Mojave earthquake line: a new fault system?* (Vol. 3) (No. 10).

Nur, A., Ron, H., & Scottti, O. (1989). Kinematics and Mechanics of Tectonic Block Rotations. *Geophysical*, *49*, 31–46.

Oppenheimer, D. H., Bakun, W. H., & Lindh, A. G. (1990). Slip Partitioning of the Calaveras Fault, California, and Prospects for Future Earthquakes. *Journal of Geophysical Research*, *95*(90), 8483–8498.

Peacock, D. C. (1991). Displacements and segment linkage in strike-slip fault zones. *Journal of Structural Geology*, *13*(9), 1025–1035. doi: 10.1016/0191-8141(91)90054-M

Peacock, D. C., & Sanderson, D. J. (1996). Effects of propagation rate on displacement variations along faults. *Journal of Structural Geology*, *18*(2-3), 311–320.

doi: 10.1016/S0191-8141(96)80052-6

Perrin, C., Manighetti, I., Ampuero, J.-P., Cappa, F., & Gaudemer, Y. (2016). Location of largest earthquake slip and fast rupture controlled by along-strike change in fault structural maturity due to fault growth. *Journal of Geophysical Research: Solid Earth RESEARCH*, *2*, 1–16. doi: 10.1002/2012JB010016.1.

Perrin, C., Manighetti, I., & Gaudemer, Y. (2016). Off-fault tip splay networks: A genetic and generic property of faults indicative of their long-term propagation. *Comptes Rendus - Geoscience*, *348*(1), 52–60. doi: 10.1016/j.crte.2015.05.002

Plesch, A., Nicholson, C., Shaw, J., Marshall, S., Su, M.-H., & Maechling, P. (2017). *The SCEC Community Fault Model (CFM).* Retrieved from `https://www.scec.org/research/cfm`

Plesch, A., Shaw, J. H., Benson, C., Bryant, W. A., Carena, S., Cooke, M., … Yeats, R. (2007). Community Fault Model (CFM) for southern California. *Bulletin of the Seismological Society of America*, *97*(6), 1793–1802. doi: 10.1785/0120050211

Poliakov, A. N. B., Dmowska, R., & Rice, J. R. (2002). Dynamic shear rupture interactions with fault bends and off-axis secondary faulting. *Journal of Geophysical Research: Solid Earth*, *107*(B11), ESE 6–1–ESE 6–18. Retrieved from `http://doi.wiley.com/10.1029/2001JB000572` doi: 10.1029/2001JB000572

Preuss, S., Herrendörfer, R., Gerya, T., Ampuero, J., & van Dinther, Y. (2018). Model data set and video to "Seismic and aseismic fault growth lead to different fault orientations". Retrieved from `https://www.research-collection.ethz.ch/handle/20.500.11850/307985` doi: https://doi.org/10.3929/ethz-b-000307985

Regenauer-Lieb, K., Hobbs, B., Yuen, D. A., Ord, A., Zhang, Y., Mulhaus, H. B., & Morra, G. (2006). From point defects to plate tectonic faults. *Philosophical Magazine*, *86*(21-22), 3373–3392. doi: 10.1080/14786430500375159

Regenauer-Lieb, K., & Yuen, D. A. (2003). Modeling shear zones in geological and planetary sciences: Solid- and fluid-thermal-mechanical approaches. *Earth-Science Reviews*, *63*(3-4), 295–349. doi: 10.1016/S0012-8252(03)00038-2

Ross, Z. E., Hauksson, E., & Ben-Zion, Y. (2017). Abundant off-fault seismicity and orthogonal structures in the San Jacinto fault zone. *Science Advances*.

Rubin, A. M., & Ampuero, J. P. (2005). Earthquake nucleation on (aging) rate and state faults. *Journal of Geophysical Research: Solid Earth*, *110*(11), 1–24. doi: 10.1029/2005JB003686

Ruina, A. (1983). Slip instability and state variable friction laws. *Journal of Geophysical Research*, *88*(B12), 10359–10370. doi: 10.1029/JB088iB12p10359

Schaff, D. P., & Beroza, G. C. (2004). Coseismic and postseismic velocity changes measured by repeating earthquakes. *Journal of Geophysical Research: Solid Earth*, *109*(10). doi: 10.1029/2004JB003011

Scholz, C. H. (2000). Evidence for a strong San Andreas fault. *Geology*, *28*(2), 163–166. Retrieved from `http://geology.gsapubs.org/content/28/2/163` doi: 10.1130/0091-7613(2000)28⟨163:EFASSA⟩2.0.CO;2

Scholz, C. H., Ando, R., & Shaw, B. E. (2010). The mechanics of first order splay faulting: The strike-slip case. *Journal of Structural Geology*, *32*(1), 118–126. Retrieved from `http://dx.doi.org/10.1016/j.jsg.2009.10.007` doi: 10.1016/j.jsg.2009.10.007

Scholz, C. H., & Lawler, T. M. (2004). Slip tapers at the tips of faults and earthquake ruptures. *Geophysical Research Letters*, *31*(21), 1–4. doi: 10.1029/2004GL021030

Segall, P., & Pollard, D. D. (1983). Nucleation and growth of strike slip patterns in Granite. *Journal of Geophysical Research*, *88*(2), 555–568.

Sibson, R., Ghisetti, F., & Ristau, J. (2011). Stress Control of an Evolving Strike-Slip Fault System during the 2010-2011 Canterbury, New Zealand, Earthquake Sequence. *Seismological Research Letters*, *82*(6), 824–832. Retrieved from `http://srl.geoscienceworld.org/cgi/doi/10.1785/gssrl.82.6.824` doi: 10.1785/gssrl.82.6.824

Sibson, R. H. (1990). Rupture nucleation on unfavorably oriented faults. *Bulletin of the Seismological Society of America*, *80*(6), 1580–1604. Retrieved from `http://www.bssaonline.org/content/80/6A/1580.short` doi: 10.1021/jp111520r

Sibson, R. H. (1994). An assessment of field evidence for 'Byerlee' friction. *Pure and Applied Geophysics PAGEOPH*, *142*(3-4), 645–662. doi: 10.1007/BF00876058

Sibson, R. H., & Rowland, J. V. (2003). Stress, fluid pressure and structural permeability in seismogenic crust, North Island, New Zealand. *Geophysical Journal International*, *154*(2), 584–594. Retrieved from `http://doi.wiley.com/10.1046/j.1365-246X.2003.01965.x` doi: 10.1046/j.1365-246X.2003.01965.x

Simpson, R. W. (1997). Quantifying Anderson's fault types. *Journal of Geophysical Research*, *102*(B8), 17909–17919.

Socquet, A., Valdes, J. P., Jara, J., Cotton, F., Walpersdorf, A., Cotte, N., … Norabuena, E. (2017). An 8month slow slip event triggers progressive nucleation of the 2014 Chile megathrust. *Geophysical Research Letters*, *44*(9), 4046–4053. doi: 10.1002/2017GL073023

Stein, R. S., King, G. C. P., & Lin, J. (1992). Change in Failure Stress on the Southern San Andreas Fault System Caused by the 1992 Magnitude = 7.4 Landers Earthquake. *Science*, *258*(5086), 1328–1332.

Townend, J., & Zoback, M. D. (2004). Regional tectonic stress near the San Andreas fault in central and southern California. *Geophysical Research Letters*, *31*(15), 1–5. doi: 10.1029/2003GL018918

Twiss, R. J., & Moores, E. M. (1992). *Structural Geology*. W.H. Freeman. Retrieved from `https://books.google.ch/books?id=eRB2QgAACAAJ`

van Dinther, Y., Gerya, T., Dalguer, L. A., Corbi, F., Funiciello, F., & Mai, P. M. (2013). The seismic cycle at subduction thrusts: 2. Dynamic implications of geodynamic simulations validated with laboratory models. *Journal of Geophysical Research: Solid Earth*, *118*(4), 1502–1525. doi: 10.1029/2012JB009479

van Dinther, Y., Gerya, T., Dalguer, L. A., Mai, P. M., Morra, G., & Giardini, D. (2013). The seismic cycle at subduction thrusts: Insights from seismo-thermo-mechanical models. *Journal of Geophysical Research: Solid Earth*, *118*(12), 6183–6202. doi: 10.1002/2013JB010380

Veedu, D. M., & Barbot, S. (2016). The Parkfield tremors reveal slow and fast ruptures on the same asperity. *Nature*, *532*(7599), 361–365. Retrieved from `http://www.nature.com/doifinder/10.1038/nature17190` doi: 10.1038/nature17190

Vermeer, P. A. (1990). The orientation of shear bands in biaxial tests. *Géotechnique*, *40*(2), 223–236. Retrieved from `https://doi.org/10.1680/geot.1990.40.2.223` doi: 10.1680/geot.1990.40.2.223

Weng, H., & Yang, H. (2017). Seismogenic width controls aspect ratios of earthquake ruptures. *Geophysical Research Letters*, *44*(6), 2725–2732. doi: 10.1002/2016GL072168

Willemse, E. J. M., & Pollard, D. D. (1998). On the orientation and patterns of wing cracks and solution surfaces at the tips of a sliding flaw or fault. *Journal of Geophysical Research: Solid Earth*, *103*(B2), 2427–2438. Retrieved from `http://doi.wiley.com/10.1029/97JB01587` doi: 10.1029/97JB01587

Woodcock, N. H., & Fischer, M. (1986). Strike-slip duplexes. *Journal of Structural Geology*, *8*(7), 725–735. doi: 10.1016/0191-8141(86)90021-0

Xu, S., & Ben-Zion, Y. (2013). Numerical and theoretical analyses of in-plane dynamic rupture on a frictional interface and off-fault yielding patterns at different scale. *Geophysical Journal International*, *193*(1), 304–320. doi: 10.1093/gji/ggs105

Zang, A., & Stephansson, O. (2010). *Stress Field of the Earth's Crust*. Dordrecht: Springer Netherlands. Retrieved from `http://link.springer.com/10.1007/978-1-4020-8444-7` doi: 10.1007/978-1-4020-8444-7

Zoback, M., Hickman, S., & Ellsworth, W. (2010). Scientific drilling into the San Andreas fault zone. *Eos Trans. AGU*, *91*(22), 197–204. Retrieved from `http://www.agu.org/pubs/eos-news/supplements/2010/zoback{_}91{_}22.shtml`

Zoback, M. D. (1991). State of stress and crustal deformation along weak transform faults. *Philosophical Transactions - Royal Society of London, A*, *337*(1645), 141–150. doi: 10.1098/rsta.1991.0112

Zoback, M. D., Zoback, M. L., Mount, V. S., Suppe, J., Eaton, J. P., Healy, J. H., ... Wentworth, C. (1987). New Evidence on the State of Stress of the San Andreas Fault System. *Science,*, *238*(4830), 1105–1111.